Editors' Suggestion

Anatomy of spin-orbit torques in monolayer Fe_3GeTe_2 and Fe_3GaTe_2: Insights from atomistic and momentum-space decompositions

Gusthavo M. S. Brizolla [1,*] Stepan S. Tsirkin [2] Yaroslav Zhumagulov [2] and Jaroslav Fabian [1,3]

[1]*Institute of Theoretical Physics, University of Regensburg, 93053 Regensburg, Germany*

[2]*Institute of Physics, École Polytechnique Fédérale de Lausanne (EPFL), CH-1015 Lausanne, Switzerland*

[3]*Halle-Berlin-Regensburg Cluster of Excellence CCE, University of Regensburg, 93040 Regensburg, Germany*

(Received 5 August 2026; accepted 9 October 2026; published 22 October 2026)

We present a systematic first-principles study of the spin-orbit torques in the ferromagnetic monolayers Fe_3GeTe_2 (FGT) and Fe_3GaTe_2 (FGaT). Despite sharing the same crystal structure (point group D_{3h}) and predominantly Fe 3*d* spin-polarized bands, the two materials exhibit markedly different current-induced torques. We reveal these differences by computing the full angular dependence of the torkance—the torque per unit applied electric field—using linear-response theory with symmetry-adapted spin-orbit-coupled Wannier functions. FGaT may be viewed as a hole-doped analog of FGT, since Ga contributes one valence electron fewer than Ge. Although the work functions differ by only about 28 meV, the band filling near K and K' changes substantially: The density of states at ε_F is reduced by a factor of 3 and its spin polarization reverses from minority in FGT to majority in FGaT. These electronic changes are reflected in the torques resolved by time-reversal parity, sublattice, and momentum. In particular, we identify pronounced hidden torques in FGaT and relate the suppression of its fourth-harmonic Fermi-sea component to the evolution of momentum-space pockets. Finally, we discuss the emergence of such self-torques, which are not captured by the conventional picture of current-induced spin accumulation, within a symmetry-based phenomenological framework. Our results provide microscopic insight into current-induced torques in two-dimensional ferromagnets and offer guidance for defect and van der Waals engineering of layered magnetic materials.

DOI: 10.1103/1v68-qwcl

I. INTRODUCTION

Electrical control of magnetization is a central goal of spintronics [1]. Particularly important is current-induced magnetization switching, achieved first through the spin-transfer torque predicted by Slonczewski and Berger [2–4]. An appealing alternative is the spin-orbit torque (SOT), which relies on spin-orbit coupling to induce magnetization dynamics: An electric current generates a spin accumulation [5], which exerts a torque on the magnetization [6] and, above a critical current, switches it [7–9].

Van der Waals (vdW) magnets are natural hosts for SOT physics: They remain magnetically ordered down to the monolayer [10–12], their carrier density is gate-tunable [13], and their low crystal symmetry admits torque components forbidden in high-symmetry metals [14,15]. Among layered magnetic metals, Fe_3GeTe_2 (FGT) and Fe_3GaTe_2 (FGaT) are prominent, combining itinerant ferromagnetism with strong perpendicular anisotropy. The Curie temperature of FGT, $T_C \approx 200$–$220\,\mathrm{K}$ in the bulk, drops to $\sim$70–130 K in the monolayer [12,13,16] but can be restored to room temperature by ionic gating in few-layer samples [13], while FGaT retains room-temperature ferromagnetism down to a few layers [17,18]. SOT switching has been demonstrated for both in heterostructures with heavy metals, topological insulators, and low-symmetry semimetals [19–25].

Lacking inversion symmetry in monolayer form, both compounds support a *self-torque*: an SOT generated by the spin-orbit fields of the material itself, with no interface required. However, the crystal symmetry makes their self-torque unconventional. Indeed, the horizontal mirror forbids the magnetization-independent Rashba-Edelstein field induced by electric current, so the leading spin polarization must be linear in the in-plane magnetization (which breaks the horizontal mirror symmetry) and acts as a current-induced in-plane anisotropy [26]. In centrosymmetric bulk FGT and FGaT, the corresponding fields remain "hidden", alternating from layer to layer and canceling in the net response while producing layer-resolved torques [27,28] that trace back to the local symmetry of each magnetic site [29–31].

First-principles calculations for monolayer FGT have mapped the angular dependence of the torque for both time-reversal-even and time-reversal-odd channels, revealing harmonics well beyond the leading fieldlike and dampinglike forms—with direct consequences for field-free switching—and coefficients varying strongly with the chemical potential [32]. However, the microscopic origin of this filling dependence remains unresolved. Which electronic states near the Fermi level ε_F carry the dominant torque contributions? Why are the harmonic components so sensitive to band filling? Can such changes be realized intrinsically through stoichiometric modification rather than electrostatic gating? More broadly,

*Contact author: gusthavo.brizolla@physik.uni-regensburg.de

 ©2026 American Physical Society

do inversion-asymmetric monolayers host hidden torques that are not layer-resolved, as in centrosymmetric systems, but instead emerge from the site or sublattice degrees of freedom within a single layer?

In this work, we address these questions through a comprehensive first-principles and symmetry analysis of the SOTs in monolayer FGT and FGaT. These two ferromagnets form a controlled comparison: They share the same crystal structure with point group D_{3h}, and therefore the same symmetry-allowed torque forms, as well as the same dominant Fe $3d$ character at ε_F. However, they differ by one valence electron, with FGaT effectively representing a hole-doped analog of FGT. Any qualitative difference in their torques can therefore be traced primarily to the change in band filling.

Specifically, we compute the angular dependence of the intrinsic SOTs of both monolayers using Kubo-Bastin linear response [33] with symmetry-adapted Wannier functions constructed from fully relativistic density-functional theory. Thus, spin-orbit coupling is incorporated from the outset, rather than introduced as an additional term during Wannierization. We employ a rigid rotation of the exchange field, benchmarked against self-consistent noncollinear calculations, to enable dense angular sampling of the torque landscape.

The electronic structures of FGT and FGaT are qualitatively similar, but the hole doping in FGaT leads to reduced band filling, most prominently around the K and K' points. Individual band features are shifted by up to $\sim$100 meV between the two compounds, exceeding the difference in work functions of only $\sim$30 meV. These energy scales are accessible by electrostatic or ionic gating [23,24]. The two materials also exhibit comparable valley-Zeeman splittings of about 40 meV.

Despite these electronic differences, the overall torque magnitudes remain similar. However, the pronounced fourth-harmonic contribution to the time-reversal-even torque in FGT is strongly reduced in FGaT, which we trace to the suppression of the K-point Fermi pockets. In contrast, the time-reversal-odd torques are largely transferable between the two compounds. A particularly promising route for torque engineering emerges from the hidden Rashba-Edelstein-like torques associated with the two Fe sublattices related by the horizontal mirror symmetry. In FGaT, these site-resolved torques can exceed the symmetry-allowed components by nearly a factor of 30. Although they cancel exactly in the ideal monolayer, breaking the sublattice symmetry provides a route to activate these large hidden contributions.

We organize the paper as follows. In Sec. II we present the computational framework, including the first-principles setup, symmetry-adapted Wannier construction, Kubo-Bastin torkance formalism, and rigid-rotation approach. Section III compares the electronic structures of the two monolayers (Sec. III A) and then analyzes their angular-dependent torkances (Sec. III B), including atom- and momentum-resolved contributions. Section IV discusses the symmetry-based phenomenology of the torques, followed by the conclusions in Sec. V. We leave technical details, including benchmarking, to the Appendixes.

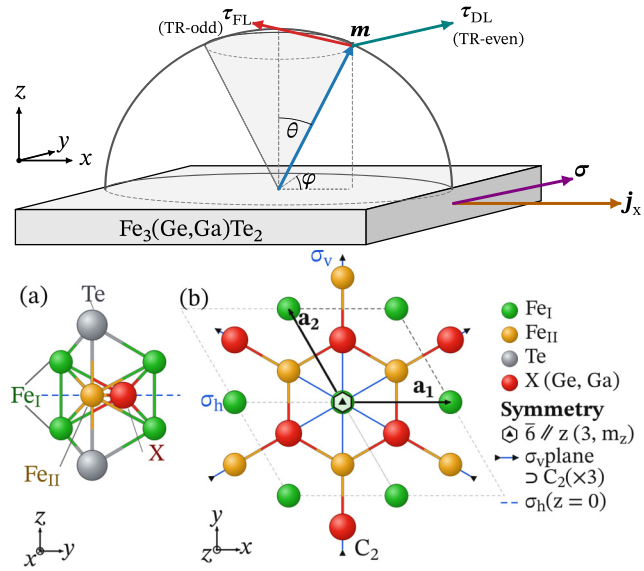


FIG. 1. Geometry and crystal structure. Top: response geometry. An in-plane field $\mathbf{E} \parallel \hat{\mathbf{x}}$ drives a current j_x; the magnetization direction $\hat{\mathbf{m}}$ is parametrized by spherical angles (θ, ϕ). The axis $\hat{\boldsymbol{\sigma}} \equiv \hat{\mathbf{z}} \times \hat{\mathbf{E}}$ and the conventional bilayer torques—fieldlike $\boldsymbol{\tau}_{\mathrm{FL}} \parallel \hat{\mathbf{m}} \times \hat{\boldsymbol{\sigma}}$ (time-reversal odd) and dampinglike $\boldsymbol{\tau}_{\mathrm{DL}} \parallel \hat{\mathbf{m}} \times (\hat{\boldsymbol{\sigma}} \times \hat{\mathbf{m}})$ (time-reversal even)—are drawn only to fix axes and nomenclature: In the D_{3h} monolayer both rigid forms are symmetry forbidden, and the leading self-torque is magnetization dependent (Sec. III A). Bottom: (a) side and (b) top views of Fe_3XTe_2, with the inequivalent sites Fe_I (green, outer planes) and Fe_{II} (amber, central plane). The nonmagnetic space group is $P\bar{6}m2$ (No. 187, point group D_{3h}); (b) marks the $\bar{6}$ axis and the three σ_v mirrors, whose traces contain the in-plane C_2 axes, and (a) the horizontal mirror σ_h (dashed).

II. COMPUTATIONAL METHODS

A. Density-functional theory

First-principles calculations were performed with QUANTUM ESPRESSO [34–36] using fully relativistic optimized norm-conserving Vanderbilt (ONCV) pseudopotentials [37] from the PSEUDODOJO library [38]. Spin-orbit coupling (SOC) was treated self-consistently in the noncollinear framework, with the magnetization initialized along $\hat{\mathbf{z}}$. The response geometry, crystal structure, unit cell, and point symmetries (D_{3h}) of monolayer Fe_3XTe_2 (X = Ge, Ga) are sketched in Fig. 1. The monolayer is a five-plane stack Te-Fe_I-(Fe_{II}, X)-Fe_I-Te with two inequivalent iron sites: the σ_h-related pair Fe_I in the outer planes, and the single Fe_{II} sharing the central plane with X. This Fe_I/Fe_{II} partition underlies the atom-resolved analysis of the SOT (Sec. III B 3). Periodic images were separated by 30 Å of vacuum, and spurious interimage Coulomb interactions were removed by a two-dimensional cutoff [39,40].

The in-plane lattice constant and internal coordinates were relaxed within the PBE-GGA [41] (residual forces $<10^{-5}$ Ry/Bohr, total-energy changes $<10^{-5}$ Ry), giving $a = 3.95$ Å (FGT) and $a = 3.88$ Å (FGaT), 1.0% and 2.7% below the bulk experimental values of 3.991 and 3.986 Å, respectively [42–44]. All subsequent electronic-structure and response calculations used the Perdew-Wang LDA [45] at this geometry:

For bulk FGT, LDA yields Fe moments within the experimental range, whereas PBE overestimates them by ∼30% to 40% [46,47], and LDA was likewise the choice of the previous first-principles SOT study of monolayer FGT [32].

Plane waves were expanded to a kinetic-energy cutoff of 120 Ry. The self-consistent cycle used a $24 \times 24 \times 1$ **k** mesh, first-order Methfessel-Paxton smearing [48] of width 0.02 Ry, and a self-consistency threshold of 10^{-8} Ry; the same mesh provides the coarse grid for the Wannier construction of Sec. II B.

B. Wannier interpolation

Brillouin zone integrals on the dense **k** meshes required for linear response were evaluated by Wannier interpolation, using symmetry-adapted Wannier functions (SAWFs) [49] built in WANNIERBERRI [50], which combines Marzari-Vanderbilt localization [51] and Souza-Marzari-Vanderbilt disentanglement [52] with symmetry constraints on the projectors. The SAWFs are constructed directly from the spinor Bloch states of Sec. II A, in which SOC is included self-consistently from the outset; the interpolated model therefore inherits the *ab initio* spin-orbital entanglement rather than acquiring SOC as an added term. The construction enforces the full magnetic space group of the $\hat{\mathbf{m}} \parallel \hat{\mathbf{z}}$ ground state, $P\bar{6}m'2'$: the symmetry elements of Fig. 1(b), with the σ_v mirrors and the in-plane C_2 axes entering only in combination with time reversal. Irreducible representations and multiplicities were verified with IRREP [53].

Each monolayer is described by $N_w = 48$ spinor functions (24 spatial orbitals $\times$ 2 spin), projected onto Fe $3d$, X p, and Te p orbitals respecting the site symmetries of the corresponding Wyckoff positions. This set spans the states within several eV of the Fermi level ε_F: The exchange splitting resides in the Fe $3d$ shell, the strongest atomic SOC on the heavy Te atoms. The s-derived bands (Te $5s$, X s) lie well below this p–d manifold, separated by a gap, and contribute negligibly to the torkance. The Wannier subspace is extracted by disentanglement within an outer window of $[-8.0,\ +5.45]$ eV about ε_F for FGT and $[-6.5,\ +6.7]$ eV for FGaT, with bands frozen up to $+1.5$ and $+1.0$ eV, respectively: The interpolated bands coincide with the *ab initio* ones throughout the occupied p–d manifold and to at least 1 eV above ε_F. Appendix D quantifies both the sensitivity to the Wannierization mesh and the residual symmetry breaking introduced by the rigid rotation of the exchange field used to sample magnetization directions away from the ground state; the interpolated operators recover the exact symmetry-protected zeros of the torkance at $\hat{\mathbf{m}} \parallel \pm\hat{\mathbf{z}}$ (Appendix E).

The converged Wannier charge centers follow the pattern dictated by site symmetry: For each symmetry-related set of functions the centroid obeys the site group exactly, pinned to the nucleus on the $\bar{6}m2$ sites ($\mathrm{Fe_{II}}$, X) and free to shift only along $\hat{\mathbf{z}}$ on the trigonal-axis sites ($\mathrm{Fe_{I}}$, Te), where it moves by at most 41 mÅ (≈1% of the in-plane lattice constant a). Individual functions within a set may displace further while preserving the set centroid: The X p_z-derived pair splits symmetrically by ±73 mÅ about the nucleus, and the largest single-function deviation is an outward shift of the Te p_z-like functions into the vacuum, ≈0.2 Å (≈5% of a), identical in the two compounds. Every Wannier function thus remains essentially attached to its parent atom, as required by the sublattice projectors of Appendix B 6. The same basis carries all operators entering the linear response—the Hamiltonian, the velocity including its Berry-connection contribution, and the spin operator from which the exchange torque is built—as detailed in Appendixes A and B.

C. Torkance: Kubo formulas

A dc electric field **E** applied in the plane of the monolayer drives the electronic system into a current-carrying state that exerts a net torque $\boldsymbol{\tau} = (\tau_x, \tau_y, \tau_z)$ on the magnetization—the nonequilibrium expectation, $\boldsymbol{\tau} = \langle\hat{\boldsymbol{\tau}}\rangle$, expectation value of the exchange-torque operator $\hat{\boldsymbol{\tau}}$ defined below. In what follows, the unhatted $\boldsymbol{\tau}$ and its components τ_a denote this macroscopic torque, whereas the microscopic operator, $\hat{\tau}_a$, and its band-basis matrix elements, $\hat{\tau}^a_{nm}$, carry a hat. To linear order in the field,

$$\tau_a(\hat{\mathbf{m}}) = \sum_b t_{ab}(\hat{\mathbf{m}})\, E_b, \qquad a \in \{x, y, z\}, \quad b \in \{x, y\}, \tag{1}$$

which defines the torkance tensor t_{ab}, the torque per unit applied electric field. We split t_{ab} into parts even and odd under magnetization reversal $\hat{\mathbf{m}} \to -\hat{\mathbf{m}}$, following the Kubo-Bastin formulation of Freimuth *et al.* [33], evaluated with a constant band broadening Γ in the Green's functions. With the shorthands $x_n = \varepsilon_{n\mathbf{k}} - \varepsilon_F$ and $g_n = x_n^2 + \Gamma^2$, where $\varepsilon_{n\mathbf{k}}$ are the band energies, the $T = 0$ even (Fermi-sea) torkance is

$$\begin{aligned} t^{\mathrm{even}}_{ab} = \frac{e\hbar}{2\pi N_k} \sum_{\mathbf{k}} \sum_{n \neq m} \mathrm{Im}\big[\hat{\tau}^a_{nm}\, v^b_{mn}\big] \\ \times \left[\frac{\Gamma\,(x_m - x_n)}{g_n\, g_m} + \frac{2\Gamma}{(x_n - x_m)\, g_m} \right. \\ \left. + \frac{2}{(x_n - x_m)^2}\, \mathrm{Im}\ln\frac{x_m - i\Gamma}{x_n - i\Gamma} \right], \end{aligned} \tag{2}$$

and the odd (Fermi-surface) torkance is

$$t^{\mathrm{odd}}_{ab} = \frac{e\hbar}{\pi N_k} \sum_{\mathbf{k}} \sum_{n,m} \frac{\Gamma^2\, \mathrm{Re}\big[\hat{\tau}^a_{nm}\, v^b_{mn}\big]}{g_n\, g_m}. \tag{3}$$

Here N_k is the number of **k** points, and $v^b_{nm} = \langle n\mathbf{k}|\hat{v}_b|m\mathbf{k}\rangle$ and $\hat{\tau}^a_{nm} = \langle n\mathbf{k}|\hat{\tau}_a|m\mathbf{k}\rangle$ are the matrix elements of the velocity and torque operators in the band basis $|m\mathbf{k}\rangle$. The odd sum runs over all ordered band pairs, including $n = m$; the ordered $n \neq m$ sum in Eq. (2) retains only the part of the bracket antisymmetric in $n \leftrightarrow m$, matching the antisymmetry of $\mathrm{Im}[\hat{\tau}^a_{nm} v^b_{mn}]$, so the second term is unambiguous despite its asymmetric form.

The torque operator $\hat{\tau}_a$ is the exchange torque: the commutator of the exchange field—the time-reversal-odd part of the Hamiltonian, which carries the dependence on the magnetization direction—with the spin operator, both in Wannier-interpolated form (Appendix B 4). Decomposing the interpolated Hamiltonian into its two time-reversal components makes the separation explicit (Appendixes B 2 and D): The odd part has a spectrum centered on zero and confined to the exchange scale, narrow compared with the full

p–d dispersion, and carries no filling of its own. Spin-orbit coupling adds to this exchange field small spin-mixing terms that do not transform as a rigid rotation of the magnetization; they are removed from the torque operator by a spin projection (Appendix B 3). The projection enters the torque operator only: Band energies, states, and velocities are those of the full, unprojected Hamiltonian at every magnetization direction (Sec. II D). The velocity operator contains, besides the band-dispersion (Peierls) term, the Berry-connection contribution required for gauge covariance of the response (Appendix A 2). The torkance is expressed in units of $e\,a_0$.

In a generic magnet the leading harmonics of the torkance—those generated by a rigid, magnetization-independent effective field—are the conventional dampinglike ($\boldsymbol{\tau}_{\mathrm{DL}}$) and fieldlike ($\boldsymbol{\tau}_{\mathrm{FL}}$) forms of Fig. 1. In the D_{3h} monolayer this shell is symmetry-empty—no such rigid field exists—so every allowed harmonic is intrinsically $\hat{\mathbf{m}}$ dependent and the angular dependence carries higher harmonics (Sec. III A) [26,32]. We therefore use even and odd—the time-reversal parity—as the primary channel labels, reserving fieldlike and dampinglike for the dynamical action.

As the broadening $\Gamma \to 0$, t^{even} approaches its intrinsic interband (Berry-curvature–type) value while t^{odd} scales as $1/\Gamma$, the hallmark of a scattering-limited Fermi-surface response (Appendix C). The results reported below use $\Gamma = 10\,\mathrm{meV}$, $T = 0\,\mathrm{K}$, and an 800×800 Monkhorst-Pack $\mathbf{k}$ mesh, whose density is dictated by the Fermi-surface Lorentzians of width Γ that dominate t^{odd}; at this broadening, all torkances reported below are converged with respect to the mesh.

D. Magnetization rotation and angular dependence

The magnetization orientation is parametrized by spherical angles as $\hat{\mathbf{m}}(\theta,\phi) = (\sin\theta\cos\phi, \sin\theta\sin\phi, \cos\theta)$, with the polar angle θ measured from $\hat{\mathbf{z}}$ and the azimuthal angle ϕ from $\hat{\mathbf{x}}$; the field is fixed along $\mathbf{E} \parallel \hat{\mathbf{x}}$, as indicated in Fig. 1. Because SOC ties the electronic structure to the magnetization direction, the angular dependence of Eq. (1) would in principle require a separate self-consistent calculation and Wannierization for every orientation, which is impractical for the dense angular grids used below. One route computes the electronic structure without SOC and adds it *a posteriori* as an atomic term in the Wannier basis [32]. We, instead, retain the self-consistently coupled SOC of Sec. II A and rotate only the exchange part of the Hamiltonian.

In this rigid-exchange-rotation scheme the *ab initio* Hamiltonian is computed once, for $\hat{\mathbf{m}} \parallel \hat{\mathbf{z}}$, and split into its time-reversal-even (TR-even) and time-reversal-odd (TR-odd) parts: The former collects the orbital and spin-orbit terms, the latter is the exchange field of Sec. II C. A rotated magnetization $\hat{\mathbf{m}}$ is described by the spinor transformation

$$H_{\mathrm{odd}}(\mathbf{k};\hat{\mathbf{m}}) = U_R\, H_{\mathrm{odd}}(\mathbf{k};\hat{\mathbf{z}})\, U_R^{\dagger}, \tag{4}$$

where U_R rotates the spinor index by θ about $\hat{\mathbf{n}} = (\hat{\mathbf{z}} \times \hat{\mathbf{m}})/|\hat{\mathbf{z}} \times \hat{\mathbf{m}}|$—the SU(2) rotation that maps $\hat{\mathbf{z}} \to \hat{\mathbf{m}}$—and acts as the identity on the orbital index; the TR-even Hamiltonian is left unchanged. The TR-odd contributions to the velocity—Peierls and Berry-connection—are rotated by the same U_R, while the TR-even velocity is not (Appendixes B 3 and B 5). A single Wannierization thus serves all orientations, which avoids gauge mismatches between independent constructions and yields $t_{ab}(\theta,\phi)$ efficiently on the dense $\mathbf{k}$ meshes of Sec. II C.

Exact at the reference orientation by construction, the scheme is benchmarked away from it, point by point along a yz-plane sweep of the magnetization, against fully self-consistent noncollinear DFT: The two agree to within ∼5% over most of the sweep, with the largest deviation, ∼17%, confined to t_{zx}^{even} at $\hat{\mathbf{m}} \parallel \pm\hat{\mathbf{y}}$. The deviation reflects the residual SOC-induced dependence of the Hamiltonian on $\hat{\mathbf{m}}$ that a rigid rotation of its exchange part cannot capture—an error that grows with the SOC strength, so the scheme should be applied with care to more strongly spin-orbit-coupled magnets (Appendix E).

III. RESULTS

A. Electronic structure of monolayer Fe_3GeTe_2 and Fe_3GaTe_2

Monolayers Fe_3XTe_2 are noncentrosymmetric hexagonal layers cleaved from the centrosymmetric $P6_3/mmc$ bulk [13,17]. The point group is D_{3h} ($\bar{6}m2$), generated by the roto-reflection axis $\bar{6}$ along $\hat{\mathbf{z}}$, which comprises the threefold rotation C_3 and the horizontal mirror σ_h (the layer plane), together with three vertical mirrors σ_v, each containing an in-plane twofold axis C_2 along $\langle 210\rangle$, i.e., through $\mathrm{Fe_{II}}$ and the in-plane projections of the $\mathrm{Fe_I}$ and X sites [Fig. 1(b)]. The $\mathrm{Fe_I}$–$\mathrm{Fe_I}$ dumbbells stand perpendicular to the central $\mathrm{Fe_{II}}$–X plane [Fig. 1(a)], and the broken inversion makes a self-torque symmetry-allowed under an in-plane electric field.

Spin-orbit torque relies on the interplay of magnetic exchange and SOC and we now establish how the two monolayers differ in this respect. They share the point group D_{3h}, so the symmetry-allowed structure of their electronic and magnetic responses is identical, and the difference is band filling: Replacing Ge with Ga removes one valence electron, hole-doping the monolayer. Referenced to the vacuum level, the calculated Fermi level of FGaT lies ∼28 meV below that of FGT for $\hat{\mathbf{m}} \parallel \hat{\mathbf{z}}$, so its work function is 28 meV larger. More consequential than this global offset are the accompanying shifts of individual band features relative to ε_F, typically 30–130 meV. Figure 2 shows the fully relativistic band structures for out-of-plane and in-plane magnetization, colored by the spin projection onto $\hat{\mathbf{m}}$; comparing Figs. 2(a) and 2(c), the minority-spin pocket at K rises from $-0.44\,\mathrm{eV}$ in FGT to $-0.31\,\mathrm{eV}$ in FGaT. The spin polarization of the density of states at ε_F is likewise opposite, minority in FGT and majority in FGaT (Appendix F).

The dependence of the bands on the magnetization *direction* is entirely due to SOC. The absence of space inversion together with σ_h induces out-of-plane valley-Zeeman (Ising) spin-orbit fields of opposite sign at K and K′. For $\hat{\mathbf{m}} \parallel \hat{\mathbf{z}}$ these add to the exchange with opposite signs in the two valleys, making K and K′ inequivalent [Figs. 2(a) and 2(c)]. Rotating $\hat{\mathbf{m}}$ into the plane restores a twofold rotation that exchanges the valleys, and the corner spectra equalize [Figs. 2(b) and 2(d)]. Half the K–K′ splitting of the deep minority pocket gives a valley-Zeeman coupling of 42 meV in both compounds, with neighboring deep corner bands yielding 40–50 meV. Their near identity across the substitution shows the Ising fields to

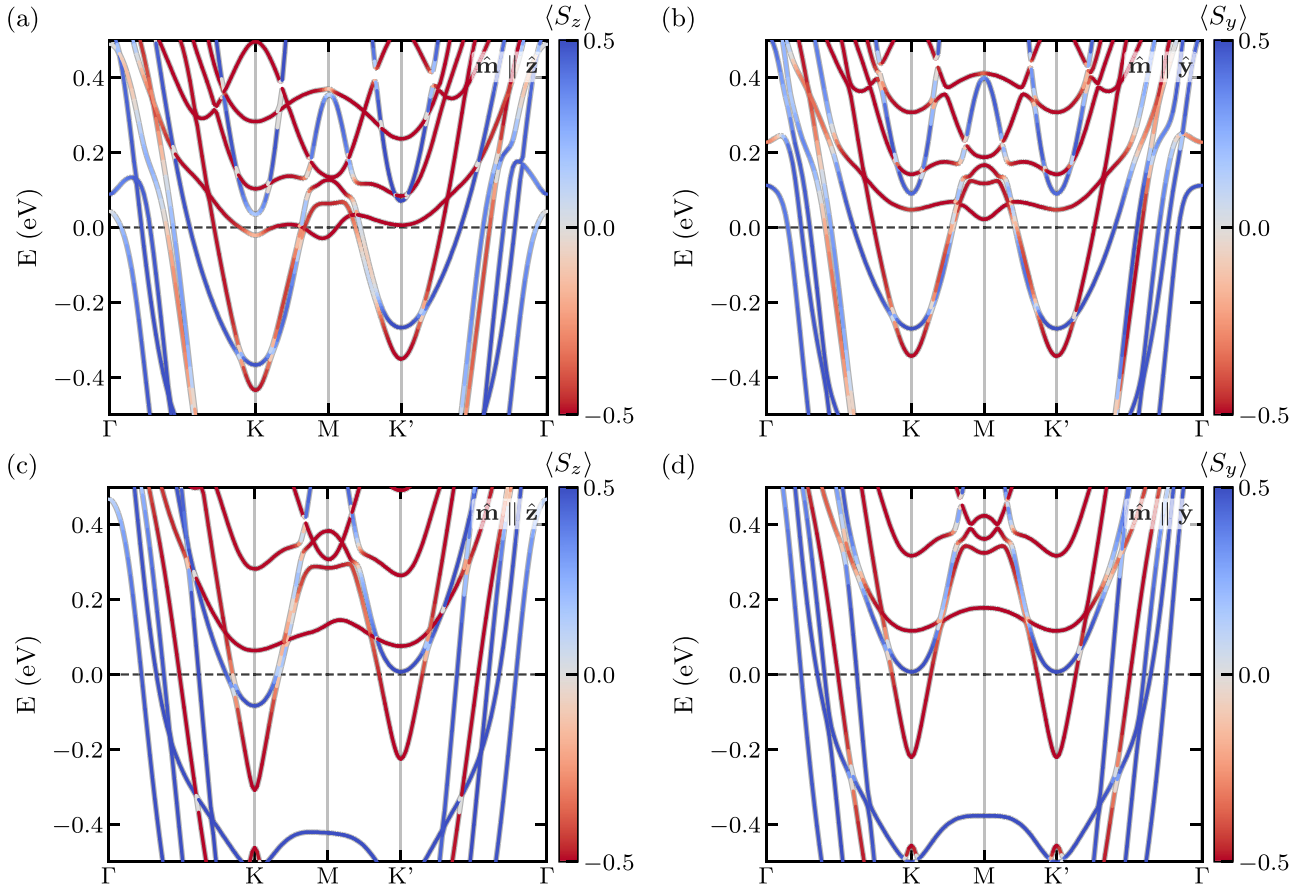


FIG. 2. Spin-projected band structures along Γ–K–M–K′–Γ for Fe_3GeTe_2 with $\hat{\mathbf{m}} \parallel \hat{\mathbf{z}}$ (a) and $\hat{\mathbf{m}} \parallel \hat{\mathbf{y}}$ (b), and for Fe_3GaTe_2 with $\hat{\mathbf{m}} \parallel \hat{\mathbf{z}}$ (c) and $\hat{\mathbf{m}} \parallel \hat{\mathbf{y}}$ (d), obtained self-consistently for each magnetization orientation with the fully relativistic LDA + SOC setup of Sec. II A. Color encodes the spin expectation value projected onto $\hat{\mathbf{m}}$: $\langle S_z \rangle$ for $\hat{\mathbf{m}} \parallel \hat{\mathbf{z}}$, $\langle S_y \rangle$ for $\hat{\mathbf{m}} \parallel \hat{\mathbf{y}}$ (in units of $\hbar$). Energies in each panel are referenced to the Fermi level of the respective compound (horizontal dashed line, $\varepsilon_F = 0$).

be set by the Te environment, which the Ge→Ga replacement leaves intact, in contrast to the filling shifts of the band features themselves. The in-plane orientation also breaks σ_h and lifts its parity protection, so band crossings present at $\hat{\mathbf{m}} \parallel \hat{\mathbf{z}}$ open into avoided crossings.

The calculated LDA ground state reproduces the experimental site-moment hierarchy and the out-of-plane easy axis of mono- and few-layer FGT [43,54]. At $\hat{\mathbf{m}} \parallel \hat{\mathbf{z}}$ the FGT moments are $2.155\,\mu_B$ on each Fe_I and $1.253\,\mu_B$ on Fe_{II}, an average of $1.854\,\mu_B$/Fe against the experimental 1.62–$1.70\,\mu_B$/Fe [47,55], a smaller overestimate than PBE. In FGaT the Fe_I moment decreases to $1.996\,\mu_B$ and Fe_{II} increases to $1.312\,\mu_B$, close to the monolayer LDA values of Ruiz *et al.* [18]; *X* and Te carry small antiparallel moments, below $0.05\,\mu_B$ throughout. Rotating $\hat{\mathbf{m}}$ into the plane changes the moments by ∼0.1% on average and the chemical potential by <0.1 meV in FGT but ≈6 meV in FGaT, reflecting the stronger sensitivity of the FGaT corner pockets to the magnetization direction.

B. Angular dependence of the torkances in Fe_3GeTe_2 and Fe_3GaTe_2

We now present the main results of this work: the full angular dependence of the torkances, sampled over the magnetization sphere with the rigid-exchange-rotation scheme of Sec. II D applied to the Wannier models of Sec. II B and the Kubo formulas of Sec. II C. We first fix the notation used to extract the angular components. With the field direction fixed, $\mathbf{E} = E_x\hat{\mathbf{x}}$ (Fig. 1), the torkance is a single vector field on the magnetization sphere,

$$\boldsymbol{\tau}(\hat{\mathbf{m}}) = E_x\,\mathbf{t}_x(\hat{\mathbf{m}}), \quad \mathbf{t}_x \equiv (t_{xx},\, t_{yx},\, t_{zx}), \tag{5}$$

everywhere tangent to it, since $\boldsymbol{\tau} \perp \hat{\mathbf{m}}$. Each element decomposes as $t_{ab} = t_{ab}^{\text{even}} + t_{ab}^{\text{odd}}$ into the Fermi-sea (TR-even) and Fermi-surface (TR-odd) channels of Eqs. (2) and (3). We further project $\mathbf{t}_x$ onto the tangent frame of the sphere, spanned by the polar and azimuthal unit vectors $\hat{\mathbf{e}}_\theta = \partial_\theta\hat{\mathbf{m}}$ and $\hat{\mathbf{e}}_\phi = (\sin\theta)^{-1}\partial_\phi\hat{\mathbf{m}}$ of the parametrization $\hat{\mathbf{m}}(\theta,\phi)$ of Sec. II D:

$$t_\theta = \mathbf{t}_x \cdot \hat{\mathbf{e}}_\theta, \quad t_\phi = \mathbf{t}_x \cdot \hat{\mathbf{e}}_\phi. \tag{6}$$

The frame is undefined at the poles $\hat{\mathbf{m}} = \pm\hat{\mathbf{z}}$, but the torkance vanishes there exactly. Finally, because $\hat{\mathbf{e}}_\theta \to +\hat{\mathbf{e}}_\theta$ and $\hat{\mathbf{e}}_\phi \to -\hat{\mathbf{e}}_\phi$ under reversal $(\theta,\phi) \to (\pi-\theta,\phi+\pi)$, the superscripts in $t_{\theta,\phi}^{\text{even/odd}} = \mathbf{t}_x^{\text{even/odd}} \cdot \hat{\mathbf{e}}_{\theta,\phi}$ refer to the Cartesian channels, not to the parity of the scalar components: t_θ^{even} and t_ϕ^{odd} are even scalar fields on the sphere, while t_ϕ^{even} and t_θ^{odd} are odd and these last two are precisely the combinations that vanish identically on the equator.

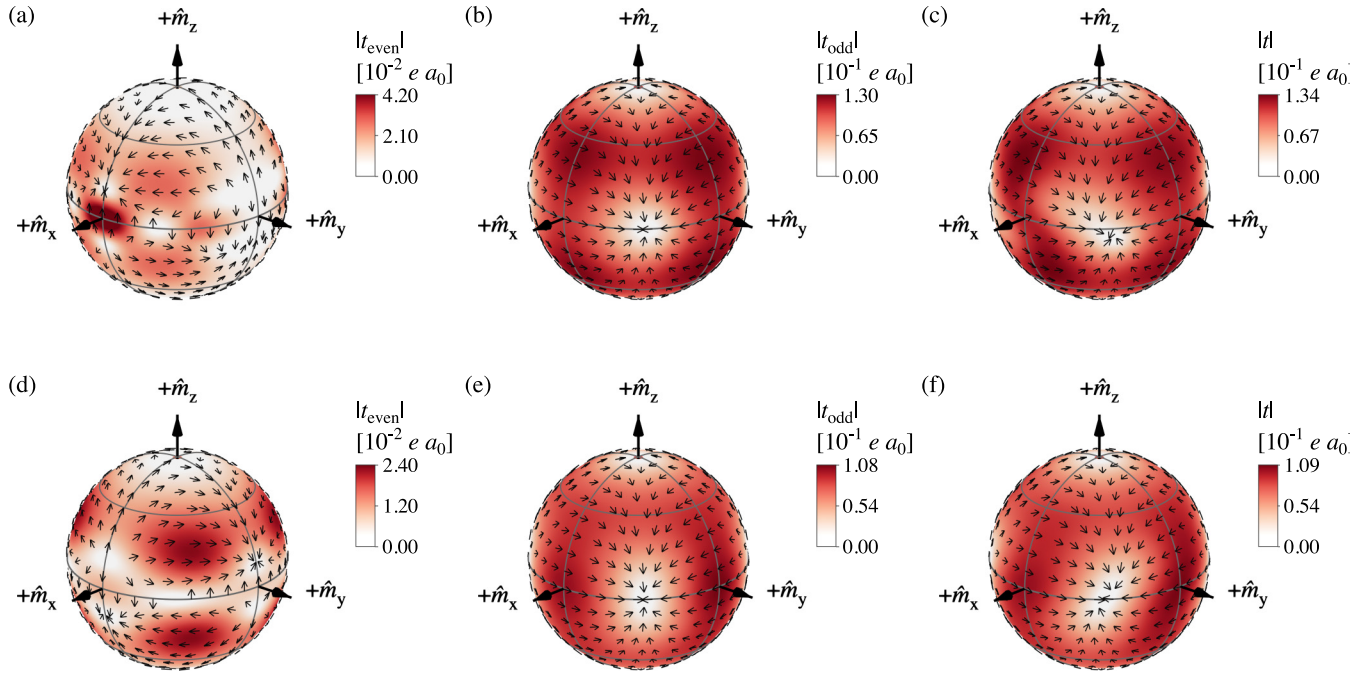


FIG. 3. Angular dependence of the spin-orbit torkance on the unit sphere of magnetization directions for monolayer Fe_3GeTe_2 [(a)–(c)] and Fe_3GaTe_2 [(d)–(f)], for $\mathbf{E} \parallel \hat{\mathbf{x}}$, $\Gamma = 10$ meV, on an 800×800 Monkhorst-Pack mesh, at the Fermi level of each compound. (a),(d) show the magnitude $|\mathbf{t}_x^{\text{even}}| = [(t_\theta^{\text{even}})^2 + (t_\phi^{\text{even}})^2]^{1/2}$ of the TR-even (Fermi-sea) channel; (b),(e) the TR-odd (Fermi-surface) $|\mathbf{t}_x^{\text{odd}}|$; (c),(f) the total $|\mathbf{t}_x|$ [Eqs. (5) and (6)]. Color encodes the magnitude; arrows give the tangent-plane direction of the displayed torkance.

1. Full-sphere overview

We plot the calculated torkances for FGT and FGaT in Fig. 3. For magnetization along $\pm\hat{\mathbf{z}}$, the torque vanishes, given the presence of the σ_h mirror. Once the magnetization tilts, σ_h is no longer a symmetry of the magnetic configuration, allowing the emergence of torque [32].

The TR-odd torkances exceed the TR-even ones in peak magnitude by factors of 2.5 (FGT) and 4.7 (FGaT). Along the equator, the two split by symmetry: The TR-even channel resides entirely in t_θ^{even} and the TR-odd channel in t_ϕ^{odd}. The TR-odd maps for FGT and FGaT are similar (the peak magnitude is ≈15% smaller in FGaT), which is a bit surprising given the rather distinct band configuration at the Fermi surfaces, (Fig. 2). However, the TR-even torkances differ markedly: The FGT peak is about twice the FGaT one, the overall sign is reversed between the compounds, and the FGT channel is strongly peaked at $\hat{\mathbf{m}} \parallel \pm\hat{\mathbf{x}}$ and nearly vanishing at $\pm\hat{\mathbf{y}}$, whereas the FGaT channel remains uniformly small on the equator, about five times below the FGT peak. Both features are analyzed by the harmonic expansion of Sec. III B 2.

The total torkances [Figs. 3(c) and 3(f)], unlike the parity-resolved channels, are not mirror-symmetric about the xz and yz planes: The magnitudes of the even and odd channels are separately symmetric under these reflections of $\hat{\mathbf{m}}$, but the two channels transform with opposite signs under the antiunitary operations $\sigma_v\hat{\Theta}$ and $C_2\hat{\Theta}$, so their interplay in $|\mathbf{t}_x|$ results in the asymmetry of the total magnitude reaching ≈35% (FGT) and ≈30% (FGaT) of the peak. On the equator, the total torkance does not vanish for any azimuthal angle—its minimum, near the diagonals, is 18% of the peak in FGT and 7% in FGaT. The true zeros lie off the equator: In FGT the magnitude drops to 3% of the peak one grid spacing below it ($\theta \approx 95^\circ$, $\phi \approx 50^\circ$), resolving the out-of-equator zero-torkance points found for monolayer FGT by Xue *et al.* [32]; in FGaT any such zero lies within one grid spacing of the equator at our 5° resolution.

2. Symmetry expansion and closed forms

We decompose the torkance over the magnetization sphere in the vector-spherical-harmonics (VSH) basis generated by two scalar potentials $\psi(\hat{\mathbf{m}})$ and $\chi(\hat{\mathbf{m}})$. Expanding these in spherical harmonics $Y_{\ell m}(\hat{\mathbf{m}})$ gives the two tangent families $\mathbf{\Psi}_{\ell m} = \nabla_s Y_{\ell m}$ and $\mathbf{\Phi}_{\ell m} = \hat{\mathbf{m}} \times \nabla_s Y_{\ell m}$, with ∇_s the surface gradient [32,56]. The torkance vectors can then be expressed as

$$\mathbf{t}_x = \nabla_s\psi + \hat{\mathbf{m}} \times \nabla_s\chi = \sum_{\ell \geqslant 1} \sum_{m=-\ell}^{\ell} [\psi_{\ell m}\, \mathbf{\Psi}_{\ell m} + \chi_{\ell m}\, \mathbf{\Phi}_{\ell m}], \quad (7)$$

where ℓ and m are the degree and azimuthal order of the scalar harmonics. Equation (7) holds for any magnet and any crystal symmetry: For a rigid, magnetization-independent field $\mathbf{b}$, the potential $\psi = \hat{\mathbf{m}} \cdot \mathbf{b}$ generates the dampinglike form $\hat{\mathbf{m}} \times (\hat{\mathbf{m}} \times \mathbf{b})$ and $\chi = \hat{\mathbf{m}} \cdot \mathbf{b}$ the fieldlike $\hat{\mathbf{m}} \times \mathbf{b}$, so the $\ell = 1$ channel would describe the Rashba spin accumulation effect. The TR-even torkance is described by the χ harmonics of even ℓ, and the ψ harmonics of odd ℓ; the TR-odd torkance by the corresponding complements [32].

Xue *et al.* [32] showed that the monolayer-FGT torque exhibits vector spherical harmonics beyond the leading shell, the higher-order terms controlling the field-free switching trajectory. We recover that content as the $m = 4$ pair of the TR-even channel, assign it to Fe_I (see the following section), and show that it is significantly reduced in FGaT.

TABLE I. Expansion coefficients of Eq. (10) for $\mathbf{E} \parallel \hat{\mathbf{x}}$, in units of $e\,a_0$, extracted from the torkance computed on the magnetization sphere (broadening $\Gamma = 10$ meV, 800×800 Monkhorst-Pack k mesh, 37×72 grid in the polar and azimuthal angles). Coefficients refer to the unnormalized basis of Eq. (7). For the unit-normalized convention of Ref. [32], $C^F_{\ell m} = \sqrt{\ell(\ell+1)}\,\chi_{\ell m}$ and $C^D_{\ell m} = \sqrt{\ell(\ell+1)}\,\psi_{\ell m}$.

	FGT	FGaT
TR-odd (Fermi surface)		
$\psi^s_{2,2}$	+0.1387	+0.1074
$\chi^c_{3,2}$	+0.0243	+0.0129
TR-even (Fermi sea)		
$\chi^s_{2,2}$	−0.0071	+0.0104
$\psi^c_{3,2}$	+0.0123	−0.0097
$\chi^s_{4,2}$	+0.0026	−0.0024
$\psi^c_{5,2}$	−0.0045	+0.0028
$\chi^s_{4,4}$	+0.0010	−0.0011
$\psi^c_{5,4}$	+0.0039	+0.0004

In Table I we give the lowest expansion coefficients calculated for FGT and FGaT, grouped by symmetric and antisymmetric combinations of the spherical harmonics with $m > 0$,

$$\mathbf{\Psi}^c_{\ell,m} = \frac{1}{\sqrt{2}}(\mathbf{\Psi}_{\ell,m} + \mathbf{\Psi}_{\ell,-m}), \tag{8}$$

$$\mathbf{\Psi}^s_{\ell,m} = \frac{1}{i\sqrt{2}}(\mathbf{\Psi}_{\ell,m} - \mathbf{\Psi}_{\ell,-m}), \tag{9}$$

and likewise for $\mathbf{\Phi}^{c,s}_{\ell,m}$, which result in real sin-like (s) and cos-like (c) functions of the azimuthal angle ϕ for the even m that occur here. In terms of these lowest harmonics, the explicit expansion reads

$$\begin{aligned}\mathbf{t}^{\text{odd}}_x &\simeq \psi^s_{2,2}\mathbf{\Psi}^s_{2,2} + \chi^c_{3,2}\mathbf{\Phi}^c_{3,2},\\ \mathbf{t}^{\text{even}}_x &\simeq \chi^s_{2,2}\mathbf{\Phi}^s_{2,2} + \psi^c_{3,2}\mathbf{\Psi}^c_{3,2}\\ &\quad + \chi^s_{4,2}\mathbf{\Phi}^s_{4,2} + \psi^c_{5,2}\mathbf{\Psi}^c_{5,2}\\ &\quad + \chi^s_{4,4}\mathbf{\Phi}^s_{4,4} + \psi^c_{5,4}\mathbf{\Psi}^c_{5,4}.\end{aligned} \tag{10}$$

These expressions can be employed to model the current-induced magnetization dynamics with the Landau-Lifshitz-Gilbert equation. They encode both the azimuthal multipoles as well as the polar anisotropy of the torques. We note that, due to D_{3h} symmetry, the allowed torque begins at $\ell = 2$ with azimuthal indices restricted to $m = 6n \pm 2$ [32].

3. *Atom- and momentum-resolved torkances*

Having analyzed the torques for the monolayers, let us now look at how the torques affect the magnetization of the individual atoms. This is particularly useful in order to see how the atoms work together to induce the magnetization dynamics. The atom-resolved torques are in general richer, especially if the atomic sites are not at high-symmetry positions, which can lead to hidden torques [29,30]. Such an analysis could facilitate atomic design of SOT via defect and van der Waals engineering.

We resolve the torkances onto the Fe_I pair, Fe_II, Te, and X sublattices (Fig. 4; consult Fig. 1 for the geometry); the two Fe_I atoms are connected by σ_h. The angular dependences depend strongly on the magnetization orientation cuts through the unit spheres, but we can observe that one of the main differences between FGT and FGaT is the opposite contributions (except for the yz plane) of the Fe_I and Fe_II atoms to the torques. It is not possible to trace this dependence to the band structure features; we rather present this as a numerical observation. In most cases Fe_II contributes most strongly, although the peak magnitudes for the Fe_I and Fe_II atoms are similar for the FGaT at the xz and xy plane.

As for the full monolayers, it is the odd torkances that dominate. The same can be said of the atom-resolved quantities. Interestingly, while Te atoms also contribute, for example in FGT in yz and xz planes, a much stronger effect comes from Ga, see for example the odd torkance in xz and xy planes.

We analyze more closely the case of the Fe_I atom pairs. The two atoms are related by the horizontal mirror. While they are equivalent for out-of-plane magnetization, as soon as $\hat{\mathbf{m}}$ tilts to the plane, the atoms are no longer equivalent [27]. From a physics perspective, one could expect a hidden spin-orbit field, equal in magnitude but antiparallel, at the two atoms, induced by the electric current. Indeed, removing σ_h allows the following spin accumulation at the two atoms, top and bottom,

$$\boldsymbol{\sigma}^{(0)}_{\text{top}} = \lambda\,\hat{\mathbf{z}} \times \mathbf{E}, \qquad \boldsymbol{\sigma}^{(0)}_{\text{bot}} = -\lambda\,\hat{\mathbf{z}} \times \mathbf{E}, \tag{11}$$

with a real parameter λ. Considering both atoms, the spin accumulation vanishes. However, this hidden spin accumulation induces hidden torques, opposite at the two atoms.

These Rashba-like spin polarizations are independent of the magnetization direction. Their most striking consequence is the appearance of odd θ-components in the xz plane, although such torques are forbidden by the global D_{3h} symmetry. They originate from hidden spin-orbit fields whose current-induced spin polarizations are locally perpendicular to the magnetization. In FGT the hidden θ-component is about three times larger than the symmetry-allowed ϕ-component, while in FGaT it is enhanced by nearly a factor of 30. As required by symmetry, the hidden contributions from the two Fe_I sublattices cancel exactly in the total torque. Remarkably, the two Te atoms, which are also related by σ_h, and are weakly magnetic due to the hybridization with Fe, have also staggered spin polarizations, though weaker than the Fe_I pair.

At higher order, the two Fe_I atoms respond differently to the magnetization-induced spin accumulation. Based on the geometry in Fig. 1, the symmetry-allowed spin accumulations are

$$\boldsymbol{\sigma}^{(1)}_{\text{top}} = E_x \begin{pmatrix} am_y + bm_z \\ am_x \\ cm_x \end{pmatrix}, \quad \boldsymbol{\sigma}^{(1)}_{\text{bot}} = E_x \begin{pmatrix} am_y - bm_z \\ am_x \\ -cm_x \end{pmatrix}, \tag{12}$$

where a, b, and c are real, material-dependent coefficients. Parameter a describes the D_{3h} allowed spin accumulation, common to both atoms, while b and c induce the hidden spin-orbit fields responsible for the hidden torques. Consequently, the two Fe_I atoms generally exhibit different, rather than merely opposite, torques, as observed, for example, in the yz plane for both FGT and FGaT.

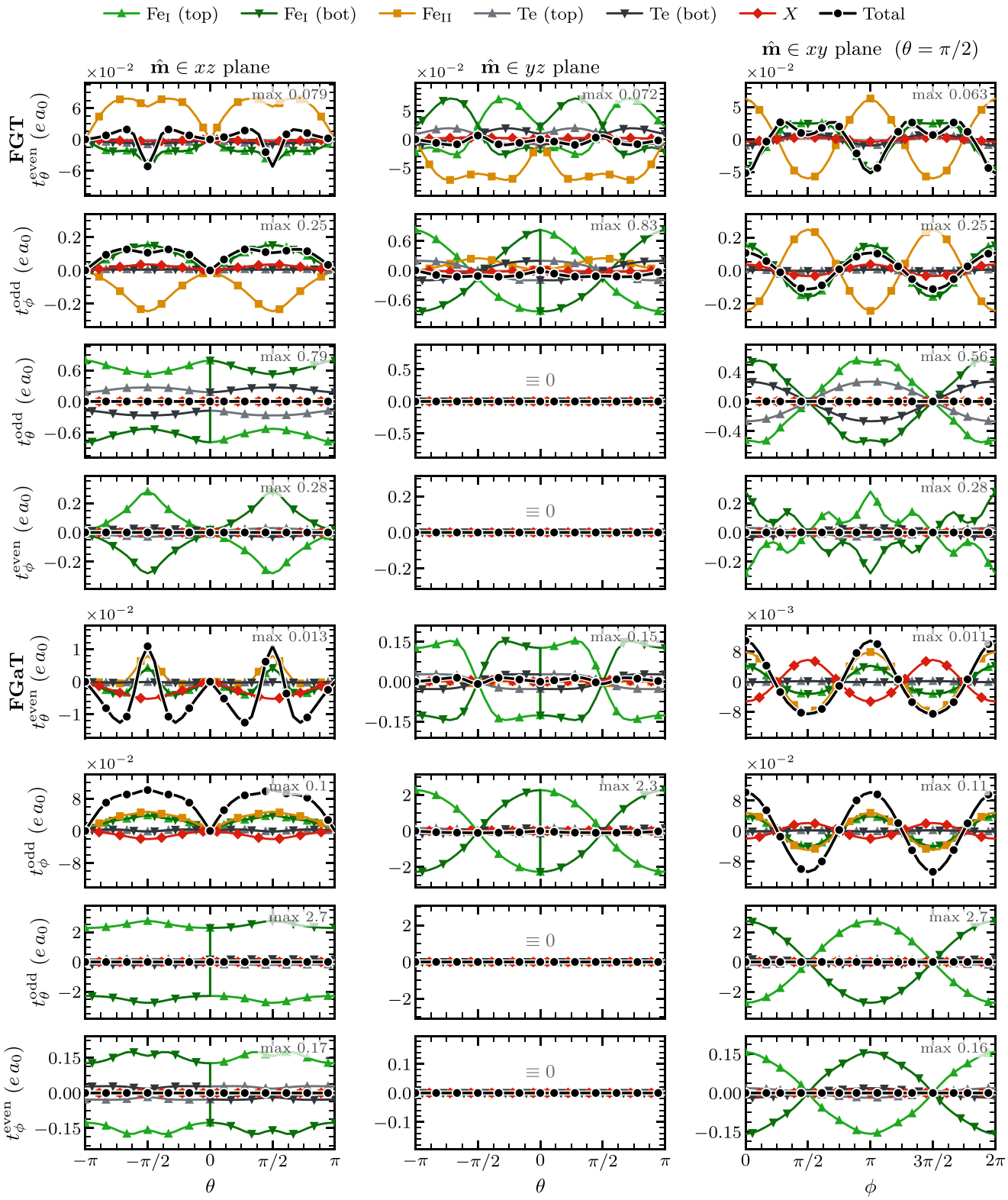


FIG. 4. Calculated atom-resolved torkance for $\mathbf{E} \parallel \hat{\mathbf{x}}$, along the xz and yz meridians and the equator $\theta = \pi/2$ (columns). For each compound the upper two rows are the channels the magnetic point group allows in the total, the lower two those it forbids. Curves give the sublattice groups and their sum (black). The forbidden channels vanish in the sum but not per site: σ_h exchanges the Fe$_I$ and Te partners and so is not a site symmetry of either, leaving their individual torques unconstrained. Fe$_{II}$ and X lie on the mirror plane, where σ_h is a site symmetry, and vanish individually. In the yz plane the vertical mirror σ_v fixes every atom, so the cancellation is site by site and those panels are identically zero. The step at $\theta = 0$ is the $\hat{\mathbf{e}}_\phi \to -\hat{\mathbf{e}}_\phi$ branch change across the pole, not a real discontinuity.

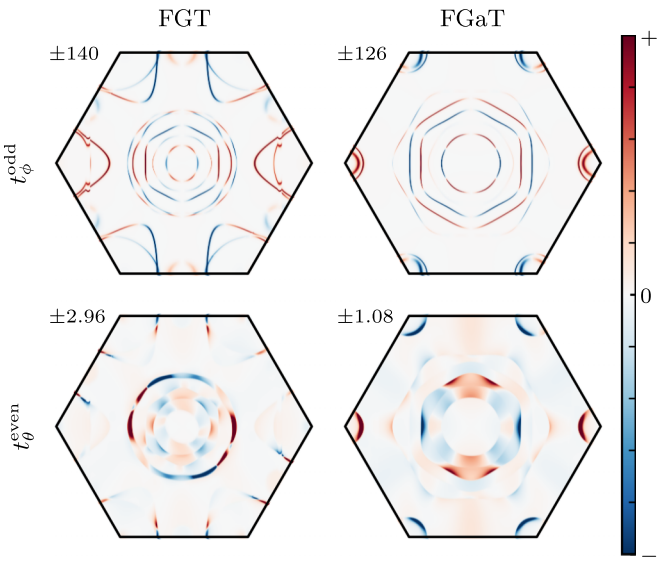


FIG. 5. Momentum-resolved torkance density for FGT (left) and FGaT (right) calculated for broadening $\Gamma = 10\,\text{meV}$ on the 800×800 mesh. The Brillouin-zone average of each panel reproduces the corresponding equatorial (xy) torkance of Fig. 4. Top: the TR-odd (fieldlike) $t_\phi^{\rm odd} = +t_{yx}^{\rm odd}$ at $\hat{\mathbf{m}} \parallel \hat{\mathbf{x}}$. Bottom: the TR-even (Fermi-sea) $t_\theta^{\rm even} = -t_{zx}^{\rm even}$ at $\phi = \pi/4$, where the $m = 2$ harmonic vanishes and the panel displays the $m = 4$ content. The diverging colorbar gives the sign (blue negative, red positive) and each panel is scaled independently to the value quoted at its upper left. The black hexagon marks the first Brillouin zone.

Figure 5 resolves the torkance densities in momentum space across the Brillouin zone. Specifically, we consider the TR-odd $t_\phi^{\rm odd}$ at $\hat{\mathbf{m}} \parallel \hat{\mathbf{x}}$, and the TR-even $t_\theta^{\rm even}$ at $\phi = \pi/4$, where $\cos 2\phi$ vanishes so that the panel displays the fourth harmonics ($m = 4$). The TR-odd density is confined to sharp contours tracing the Fermi-surface sheets. The TR-even integrand is instead spread over the zone, being strongly enhanced at band anticrossings.

The odd torkance is dominated by the Fermi-surface pockets near the K points along the k_x direction, which contribute positively to t_ϕ. Other regions of the Fermi surface exhibit alternating positive and negative torkance densities. In FGaT, the K-point pockets are smaller due to hole doping, which likely explains the somewhat reduced self-torque compared to FGT. Interestingly, these pockets also contribute to the fourth harmonic of the even torkance in FGaT, whereas their contribution is much less pronounced in FGT. However, the fourth harmonic itself, which originates predominantly from the Fe_I-derived states (see the equatorial xy-plane panels in Fig. 4, where the high-harmonic behavior is most evident), is more pronounced in FGT. This suggests that, in FGaT, the momentum-space compensation is more complete, leading to a partial cancellation of the high-harmonic contributions, as can also be inferred from Fig. 5.

IV. DISCUSSION

Both FGT and FGaT monolayers possess D_{3h} point-group symmetry. This symmetry alone forbids a current-induced spin accumulation and, consequently, a spin-orbit torque. Formally, the magnetization-independent spin accumulation,

$$\sigma_i^{(0)} = C_{ij} E_j, \tag{13}$$

vanishes identically, implying $C_{ij} = 0$. The in-plane spin accumulation is prohibited by the horizontal mirror symmetry σ_h, whereas an out-of-plane spin accumulation is forbidden by the threefold rotational symmetry C_3. As a result, neither a uniform in-plane nor an out-of-plane spin polarization can be generated by an in-plane electric field in the absence of magnetization. This does not mean that there are no hidden torques.

What is the origin of the torque we present here? The mechanism can be described as magnetization-induced spin accumulation in the presence of electric current. Indeed, a group symmetry analysis gives the spin accumulation in the first order in magnetization and electric field as

$$\sigma_i^{(1)} = C_{ijk} E_j m_k. \tag{14}$$

The third-order tensor C_{ijk} does not vanish. The mirror and rotation symmetries constrain this spin polarization to the form (obtained also from Eq. (12) by setting $b = c = 0$)

$$\boldsymbol{\sigma}^{(1)} = E_x \begin{pmatrix} a m_y \\ a m_x \\ 0 \end{pmatrix}. \tag{15}$$

While this spin polarization is still confined to the plane, as would be expected for the Rashba effect, it can be both transverse and parallel to the electric current. If the magnetization is along y, which lies in the vertical mirror plane, $\boldsymbol{\sigma}^{(1)}$ is parallel to the current. This is rather unique, not compatible with the conventional picture illustrated in Fig. 1. Certainly, being effective requires strong electric fields, but this magnetization tunability has not yet been explored in experiments.

What about out-of-plane spin accumulations? As shown above [Eq. (12)], removing the horizontal mirror symmetry unlocks out-of-plane spin components. These can generate current-induced perpendicular spin polarization and dampinglike torques, providing an additional mechanism for manipulating the magnetization. This suggests that defect engineering, as well as symmetry-reducing van der Waals heterostructures, could provide an effective route toward deterministic switching of perpendicular ferromagnets by enabling out-of-plane spin polarization and the associated spin-orbit torques.

V. CONCLUSION

We have computed the complete angular dependence of the intrinsic spin-orbit torque in monolayer Fe_3GeTe_2 and Fe_3GaTe_2 from first principles and decomposed it by time-reversal parity, atomic sublattice, and momentum, into its microscopic constituents. The two ferromagnets form a rather controlled pair, having identical crystal symmetry, the same dominant Fe $3d$ character, while differing by a single valence electron. From the calculated band structures in the presence of out-of-plane magnetization, we extracted the valley Zeeman spin-orbit fields of about 40 meV in both FGT and FGaT.

While the Fermi-surface structures of FGT and FGaT differ primarily in the size of the K-point pockets, their odd

torkances, which dominate the overall response, are remarkably similar. The odd torkance is only slightly weaker in FGaT, likely reflecting the reduced density of states associated with the smaller K-point pockets caused by hole doping. In contrast, the even torkances exhibit pronounced fourth harmonics for in-plane magnetization in FGT, whereas these higher-order harmonics are significantly suppressed in FGaT, indicating a more complete compensation of the momentum-space contributions.

The atomic decomposition also reveals hidden torques. In particular, we find that the two σ_h related atoms of the Fe_I pair exhibit different torques, which result from magnetization driven in-plane and out-of-plane spin accumulations. This is fully consistent with the symmetry arguments.

We also provide a detailed description of the computational pipeline, from density functional theory including spin-orbit coupling, through carefully symmetrized Wannier functions, to the linear-response formalism, highlighting several subtleties of the methodology, such as the use of rigid spin rotation to construct the spherical torque maps. In the Appendixes, we present a transparent account of the computational workflow together with convergence benchmarks, with the aim of facilitating the implementation and reproducibility of these calculations.

ACKNOWLEDGMENTS

This project was supported by the European Union's Horizon Europe research and innovation programme through the Graphene Flagship project 2DSPIN-TECH (Grant Agreement No. 101135853) and by the Deutsche Forschungsgemeinschaft (DFG, German Research Foundation) through SFB 1277 (Project-ID 314695032).

DATA AVAILABILITY

There are no publicly available research data or software supporting this manuscript. Requests for further information or data should be sent to the authors.

APPENDIX A: WANNIER-INTERPOLATION FORMALISM

1. Conventions and real-space matrix elements

Dense-**k** Hamiltonians, Berry connections, and velocity operators are interpolated from the coarse *ab initio* **q** mesh using the symmetry-adapted variant [49,50] of the maximally localized Wannier function (WF) formalism [52,57,58], to which we refer for the disentanglement and gauge-rotation matrices $W(\mathbf{q})$. Here these are additionally constrained by the magnetic space group, as described in Sec. II B. Two conventions specific to the present calculation are needed below.

First, the basis is fully relativistic, so the Wannier index j is a composite orbital-spin label. We order the N_w spinor WFs spin-interlaced, whereby time reversal acts as $\hat{\Theta} = (\mathbb{I}_{\text{orb}} \otimes i\sigma_y)\mathcal{K}$ with $\mathcal{K}$ complex conjugation.

Second, we use Convention II [59,60]: The Wannier centers $\bar{\mathbf{r}}_j$ are not absorbed into the Fourier phases but enter through the position matrix elements. The matrix elements of operator $\hat{O}$ in the momentum space are expanded as $O^W_{ij}(\mathbf{k}) = \sum_{\mathbf{R}} O_{ij}(\mathbf{R})\, e^{i\mathbf{k}\cdot\mathbf{R}}$. In particular, the Hamiltonian and the Wannier position matrix elements read

$$H_{ij}(\mathbf{R}) = \langle \mathbf{0}, i|H|\mathbf{R}, j\rangle, \quad \mathcal{A}_{\alpha,ij}(\mathbf{R}) = \langle \mathbf{0}, i|\hat{r}_\alpha|\mathbf{R}, j\rangle. \tag{A1}$$

Similarly for the spin operators, see Appendix B. Here i, j are composite orbital-spin Wannier indices, $\mathbf{R}$ a lattice vector, and $\alpha \in \{x, y, z\}$ a Cartesian direction; α labels the component of the position operator throughout, and hence of the Berry connection, the velocity, and the **k** derivative.

A practical point concerns the position matrix elements stored by Wannier90. The diagonal $\mathbf{R} = \mathbf{0}$ contribution corresponding to the Wannier centers is removed from the stored matrices. The Berry connection must therefore be reconstructed as

$$\mathcal{A}^W_{\alpha,ij}(\mathbf{k}) = \sum_{\mathbf{R}} \mathcal{A}^{(\text{wcc})}_{\alpha,ij}(\mathbf{R}) e^{i\mathbf{k}\cdot\mathbf{R}} + \bar{r}_{i,\alpha}\delta_{ij}, \tag{A2}$$

where $\bar{r}_{i,\alpha} = \langle \mathbf{0}, i|\hat{r}_\alpha|\mathbf{0}, i\rangle$ is the α component of the center of the ith Wannier function. Although the restored term is **k** independent, it generally does not commute with $H^W(\mathbf{k})$. Neglecting it therefore yields an incorrect velocity operator and consequently erroneous response functions.

2. Velocity operator and band basis

The velocity operator $\hat{v}_\alpha = (i\hbar)^{-1}[\hat{r}_\alpha, H]$ in the Wannier gauge can be written as [58,61]

$$v^W_\alpha(\mathbf{k}) = \frac{1}{\hbar}\partial_{k_\alpha} H^W(\mathbf{k}) + \frac{i}{\hbar}\big[H^W(\mathbf{k}), \mathcal{A}^W_\alpha(\mathbf{k})\big]. \tag{A3}$$

The first term is the group-velocity contribution. The second, geometric term carries the entire Wannier-center dependence through the diagonal of Eq. (A2) and distinguishes the proper Wannier velocity from the bare Peierls term $\partial_{k_\alpha} H^W/\hbar$ which needs to be taken into account if the centers are inequivalent. Its role has recently been underscored by Go *et al.* [62], who recast it as an orbital-dependent anomalous position and showed it to be decisive for the intrinsic orbital Hall effect. The same gauge covariance underlies the symmetry-protected torkance zeros benchmarked in Appendix E.

Diagonalizing the Wannier-gauge Hamiltonian with unitary matrix $U(\mathbf{k})$,

$$U^\dagger(\mathbf{k}) H^W(\mathbf{k}) U(\mathbf{k}) = \varepsilon(\mathbf{k}), \tag{A4}$$

defines the Hamiltonian gauge. The Berry connection in this gauge is

$$\mathcal{A}^H_\alpha = U^\dagger \mathcal{A}^W_\alpha U + i\, U^\dagger \partial_\alpha U. \tag{A5}$$

Transforming Eq. (A3) accordingly yields the standard band-basis velocity [58,61]

$$v^H_{\alpha,nm}(\mathbf{k}) = \begin{cases} \frac{1}{\hbar}\partial_{k_\alpha}\varepsilon_{n\mathbf{k}}, & n = m, \\ \frac{i}{\hbar}(\varepsilon_{n\mathbf{k}} - \varepsilon_{m\mathbf{k}})\,\mathcal{A}^H_{\alpha,nm}(\mathbf{k}), & n \neq m, \end{cases} \tag{A6}$$

where the off-diagonal velocity matrix elements are determined by the full Hamiltonian-gauge Berry connection. Together with the spin operator of Appendix B, Eqs. (A3) and (A6) provide the matrix elements required to evaluate the torkance (Appendix C).

APPENDIX B: OPERATOR CONVENTIONS AND AUXILIARY FORMULAS

1. Spin operator

For perfectly atom-centered Wannier functions the spin operator on the composite orbital ⊗ spin space of Appendix A 1 is block diagonal,

$$\hat{S}_a = \mathbb{I}_{\rm orb} \otimes S_a = \frac{\hbar}{2}\,\mathbb{I}_{\rm orb} \otimes \sigma_a, \qquad a = x, y, z, \tag{B1}$$

with σ_a the Pauli matrices, $\mathbb{I}_{\rm orb}$ the identity on the $N_{\rm orb}$-dimensional orbital subspace, and $N_w = 2N_{\rm orb}$. As WFs are typically not strictly atom-centered, we use the interpolated spin operator built from $S_{a,ij}(\mathbf{R}) = \langle \mathbf{0}, i|\hat{S}_a|\mathbf{R}, j\rangle$ (in Convention II, see Appendix A 1),

$$S^W_{a,ij}(\mathbf{k}) = \sum_{\mathbf{R}} S_{a,ij}(\mathbf{R})\, e^{i\mathbf{k}\cdot\mathbf{R}}, \tag{B2}$$

which reduces to Eq. (B1) in the atom-centered limit $S_{a,ij}(\mathbf{R}) \to \delta_{\mathbf{R},\mathbf{0}}[\hat{S}_a]_{ij}$.

Resolved on the Pauli basis, $S^W_a = \frac{\hbar}{2}\sum_b \Sigma^{(ab)}(\mathbf{k}) \otimes \sigma_b$ with $\Sigma^{(ab)} = \frac{1}{2}\mathrm{Tr}_{\rm spin}[\sigma_b S^W_a]$, where b runs over $0, x, y, z$ with $\sigma_0 = \mathbb{I}_2$ and each $\Sigma^{(ab)}$ is an orbital-space matrix in units of $\hbar/2$. A pure spin operator has $\Sigma^{(ab)} = \delta_{ab}\Sigma^W$, with Σ^W the orbital-space spin-length matrix; Eq. (B1) is the case $\Sigma^W = \mathbb{I}_{\rm orb}$.

Because the Wannier functions span only a finite subspace of the full Hilbert space, Eq. (B2) yields the spin operator projected onto the Wannier manifold. In the presence of SOC, the projected operator is no longer of the form $\mathbb{I}_{\rm orb} \otimes \sigma_a$. The deviation $\Sigma^W \neq \mathbb{I}_{\rm orb}$ therefore quantifies the SOC-induced spin mixing within the Wannier manifold.

2. Time-reversal decomposition of the Hamiltonian

With $\hat{\Theta} = U_T\mathcal{K}$ the time-reversal operator of Appendix A 1 and $U_T = \mathbb{I}_{\rm orb} \otimes i\sigma_y$ its unitary part, the time-reversed Bloch Hamiltonian is $H_{\rm TR}(\mathbf{k}) = U_T H^*(-\mathbf{k})U_T^\dagger$, and the time-reversal even and odd parts of the Hamiltonian can be introduced as

$$H_{\rm even/odd}(\mathbf{k}) = \tfrac{1}{2}[H(\mathbf{k}) \pm H_{\rm TR}(\mathbf{k})]. \tag{B3}$$

Here, $H_{\rm even}$ collects the kinetic, crystal-field, and pure spin-orbit terms while $H_{\rm odd}$ carries the entire dependence of the band structure on the magnetization direction $\hat{\mathbf{m}}$, comprising a collinear exchange contribution and SOC-induced noncollinear corrections, which are disentangled by spin-sector projection below.

In the rigid-rotation treatment adopted in the paper, the decomposition of the Hamiltonian into the even and odd terms is performed once at the reference $\hat{\mathbf{m}}_0 = \hat{z}$ and only the odd part is transformed [Eq. (B4)], with $H_{\rm even}$ held fixed. The neglected self-consistent $\hat{\mathbf{m}}$ dependence of $H_{\rm even}$ (Sec. III A) is quantified against noncollinear DFT in Appendix E.

3. Spin-sector projection of $H_{\rm odd}$

Without SOC, $H_{\rm odd}$ is block diagonal in the eigenbasis of $\hat{\mathbf{m}}\cdot\boldsymbol{\sigma}$. SOC adds TR-odd terms coupling the two spin sectors. These are physical, but they are locked to the lattice rather than following a rigid magnetization rotation, and they mix with the torque operator (Appendix B 4). We therefore project them out.

Angular sweeps parametrize $\hat{\mathbf{m}}$ by an axis-angle pair $(\hat{\mathbf{n}}, \theta)$ relative to $\hat{z}$, so that $\hat{\mathbf{m}} = R(\hat{\mathbf{n}}, \theta)\,\hat{z}$, and rotate at the operator level,

$$\begin{aligned} H_{\rm odd}(\mathbf{k}; \hat{\mathbf{m}}) &= U_R\, H_{\rm odd}(\mathbf{k}; \hat{z})\, U_R^\dagger, \\ U_R &= \mathbb{I}_{\rm orb} \otimes e^{-i\theta\,\hat{\mathbf{n}}\cdot\boldsymbol{\sigma}/2}. \end{aligned} \tag{B4}$$

Therotation acts on the *unprojected* $H_{\rm odd}$; the projection defined below is applied afterwards, at the rotated $\hat{\mathbf{m}}$.

Let $S^W_{\hat{\mathbf{m}}}(\mathbf{k}) = \hat{\mathbf{m}}\cdot\mathbf{S}^W(\mathbf{k})$, an $N_w \times N_w$ Hermitian matrix built from the interpolated spin operator [Eq. (B2)] at the unrotated $\mathbf{k}$. Its spectral decomposition

$$S^W_{\hat{\mathbf{m}}}(\mathbf{k}) = \sum_{p=1}^{N_w} s_p\, v_p v_p^\dagger \tag{B5}$$

has real eigenvalues s_p and orthonormal eigenvectors v_p, with p labeling the eigenpairs at fixed $\mathbf{k}$ (not the Wannier index of Appendix A 1). Although SOC shortens the spin ($\Sigma^W \neq \mathbb{I}_{\rm orb}$, see above), the exchange splitting keeps the spectrum bimodal: $N_{\rm orb}$ eigenvalues are positive and $N_{\rm orb}$ negative. These define the $\pm$ sectors and the orthogonal projectors

$$P_\pm(\mathbf{k}; \hat{\mathbf{m}}) = \sum_{p\,:\,s_p \gtrless 0} v_p v_p^\dagger, \qquad P_+ + P_- = \mathbb{I}_{N_w}. \tag{B6}$$

The projected Hamiltonian is

$$H^{\rm proj}_{\rm odd}(\mathbf{k}; \hat{\mathbf{m}}) = P_+ H_{\rm odd}(\mathbf{k}; \hat{\mathbf{m}})P_+ + P_- H_{\rm odd}(\mathbf{k}; \hat{\mathbf{m}})P_-, \tag{B7}$$

Hermitian and TR-odd, preserving all intrasector matrix elements and removing only the intersector entries.

The order matters: Because $\mathbf{S}^W(\mathbf{k})$ is not of the form $\mathbb{I}_{\rm orb} \otimes \boldsymbol{\sigma}$, one has $U_R P_\pm(\hat{z}) U_R^\dagger \neq P_\pm(\hat{\mathbf{m}})$, so projecting at $\hat{z}$ and then rotating is not equivalent to Eqs. (B4)–(B7). We adopt the latter, in which the sectors are defined by the exact spin operator quantized along the physical magnetization direction.

4. Exchange-torque operator

The total spin-torque operator is $\hat{\boldsymbol{\tau}}^{\rm tot} = (i/\hbar)[H, \hat{\mathbf{S}}]$. In the magnetization-frame SOT formulation [33] the relevant torque generates magnetization rotations: Under a uniform SU(2) rotation about axis a only the TR-odd part of H varies, so that

$$\left.\frac{\partial H}{\partial \theta_a}\right|_{\theta_a = 0} = \frac{i}{\hbar}\big[H_{\rm odd}, \hat{S}_a\big]. \tag{B8}$$

This presupposes that $H_{\rm odd}$ transforms rigidly under SU(2) magnetization rotations, which in the presence of SOC holds only for the projected operator of Appendix B 3. Substituting $H_{\rm odd} \to H^{\rm proj}_{\rm odd}$ and $\hat{S}_a \to S^W_a(\mathbf{k})$, so that both factors sit in the same Wannier gauge, defines the *exchange*-torque operator $\hat{\tau}_a$ of Sec. II C. Like S^W_a and v^W_α, its Wannier-gauge matrix is written without a hat and with the superscript W,

$$\tau^W_a(\mathbf{k}) = \frac{i}{\hbar}\big[H^{\rm proj}_{\rm odd}(\mathbf{k}), S^W_a(\mathbf{k})\big], \qquad a = x, y, z. \tag{B9}$$

The discarded piece $(i/\hbar)[H_{\rm even}, \hat{S}_a]$ is not a generator of magnetization rotations but a TR-even, SOC-mediated exchange

of angular momentum between spin and orbital channels and does not contribute to the magnetization-frame SOT response.

Band energies, eigenvectors, and the velocity operator are computed from the *unprojected* Hamiltonian

$$H(\mathbf{k};\hat{\mathbf{m}}) = H_{\text{even}}(\mathbf{k}) + H_{\text{odd}}(\mathbf{k};\hat{\mathbf{m}}). \tag{B10}$$

We note that the spin-sector projection enters *only* through Eq. (B9), with projectors evaluated at the target magnetization so that the projection axis tracks $\hat{\mathbf{m}}$ at every angle.

5. Velocity operator under magnetization rotation

The velocity operator also carries a TR-odd component that must be rotated consistently. Because ∂_{k_α} reverses TR parity, the Peierls derivative $\partial_\alpha H^W$ inherits a TR-odd piece from H_{even} and a TR-even piece from H_{odd}; decomposing at $\pm\mathbf{k}$ with the unitary U_T of Appendix B 2 gives

$$v_\alpha^{\text{odd/even}}(\mathbf{k}) = \tfrac{1}{2}[\partial_\alpha H^W(\mathbf{k}) \mp U_T(\partial_\alpha H^W(-\mathbf{k}))^* U_T^\dagger], \tag{B11}$$

the superscript labeling the TR parity of the velocity itself. Here v_α^{odd} originates from H_{even} and is unchanged by the magnetization rotation, while v_α^{even} originates from H_{odd} and must be rotated by U_R. Assembling the Berry-connection term of Eq. (A3) with the rotated Hamiltonian,

$$\hbar\, v_\alpha^{\text{rot}}(\mathbf{k}) = v_\alpha^{\text{odd}} + U_R\, v_\alpha^{\text{even}}\, U_R^\dagger + i\big[H(\mathbf{k};\hat{\mathbf{m}}), \mathcal{A}_\alpha^W(\mathbf{k})\big], \tag{B12}$$

where the rotated Peierls derivative is explicitly Hermitized to remove residual finite-precision asymmetry. Since $\mathcal{A}_\alpha^W$ [Eq. (A2)] is a property of the Wannier basis, independent of $\hat{\mathbf{m}}$, and does not generally commute with U_R, the last term cannot be written as a rigid SU(2) rotation of an unrotated Berry term.

6. Atom- and sublattice-resolved operators

Sublattice and orbital contributions are extracted with orthogonal Hermitian projectors $\{P_\nu\}$, diagonal in the Wannier index ν and satisfying $\sum_\nu P_\nu = \mathbb{I}_{N_w}$ and $P_\nu P_\mu = \delta_{\nu\mu} P_\nu$. Here the partition is by atomic site—the two Fe_I members, resolved individually throughout Sec. III B 3, Fe_II, the two Te sites, and the spacer (Ge/Ga)—with coarser groupings formed by summing site projectors. Because $S^W_{\hat{\mathbf{m}}}(\mathbf{k})$ carries intersite matrix elements, it does not commute with the P_ν, so the sublattice and spin-sector decompositions do not commute. We fix the order by resolving the *already* spin-sector-projected torque of Eq. (B9),

$$\tau^W_{a,\nu}(\mathbf{k}) = \tfrac{1}{2}\big\{P_\nu, \tau^W_a(\mathbf{k})\big\}, \tag{B13}$$

the symmetrization ensuring Hermiticity of each $\tau^W_{a,\nu}$. Completeness of $\{P_\nu\}$ makes the sum rule $\sum_\nu \tau^W_{a,\nu} = \tau^W_a$ exact.

APPENDIX C: KUBO FORMULAS FOR THE TORKANCE

We take $e > 0$ (electron charge $-e$), a uniform N_k-point mesh, and write

$$x_n \equiv \varepsilon_{n\mathbf{k}} - \varepsilon_F, \qquad g_n \equiv x_n^2 + \Gamma^2, \tag{C1}$$

with Γ the constant phenomenological broadening and the $\mathbf{k}$ argument suppressed. The index a labels the torque component and b the electric-field direction, identified with the velocity index α of Appendixes A and B. Band-basis matrix elements $\hat{\tau}^a_{nm}$ and v^b_{nm} follow by rotating the exchange torque [Eq. (B9)] and the full Wannier velocity [Eq. (A3); Eq. (B12) for $\hat{\mathbf{m}} \neq \hat{z}$] with the eigenvectors of $H(\mathbf{k};\hat{\mathbf{m}})$ [Eq. (B10)], so both enter the Kubo-Bastin trace in a common gauge. At zero temperature the energy integral can be performed analytically in the eigenstate basis with retarded Green's functions $G^R_n = (\varepsilon_F - \varepsilon_{n\mathbf{k}} + i\Gamma)^{-1}$, yielding the Fermi-sea and Fermi-surface contributions of Freimuth *et al.* [33],

$$t^{\text{even}}_{ab} = \frac{e\hbar}{2\pi N_k} \sum_{\mathbf{k}} \sum_{n\neq m} \text{Im}\big[\hat{\tau}^a_{nm}\, v^b_{mn}\big] \times \Bigg[\underbrace{\frac{\Gamma\,(x_m - x_n)}{g_n\, g_m}}_{\text{surface–surface}} + \underbrace{\frac{2\Gamma}{(x_n - x_m)\, g_m}}_{\text{surface–sea}} + \underbrace{\frac{2}{(x_n - x_m)^2}\, \text{Im}\ln\frac{x_m - i\Gamma}{x_n - i\Gamma}}_{\text{sea–sea}} \Bigg], \tag{C2}$$

$$t^{\text{odd}}_{ab} = \frac{e\hbar}{\pi N_k} \sum_{\mathbf{k}} \sum_{n,m} \frac{\Gamma^2\, \text{Re}\big[\hat{\tau}^a_{nm}\, v^b_{mn}\big]}{g_n\, g_m}, \tag{C3}$$

which in atomic units give the torkance in units of ea_0. This split follows from the structure of the integrand rather than from a symmetry argument, and in general need not coincide with the decomposition of the response tensor under magnetization reversal. For the magnetization-frame torque of Appendix B 4 the two do coincide—t^{even}_{ab} is even and t^{odd}_{ab} odd under $\hat{\mathbf{m}} \to -\hat{\mathbf{m}}$—and we therefore use "TR-even/Fermi-sea"

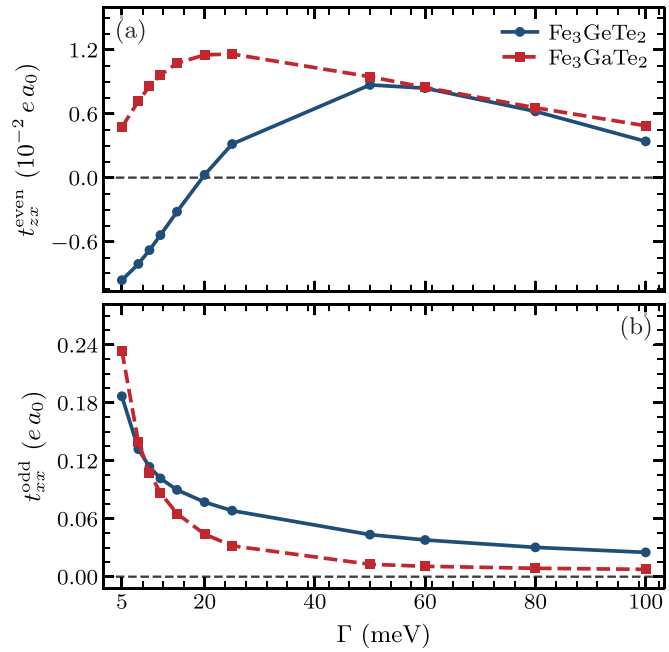


FIG. 6. Broadening dependence of the spin-orbit torkance in monolayer Fe_3GeTe_2 (blue, solid) and Fe_3GaTe_2 (red, dashed) for $\hat{\mathbf{m}} = \hat{\mathbf{y}}$ and $\mathbf{E} \parallel \hat{\mathbf{x}}$: (a) Fermi-sea contribution t^{even}_{zx} and (b) Fermi-surface contribution t^{odd}_{xx} versus the phenomenological broadening Γ, on different ordinate scales. In Fe_3GeTe_2 the dampinglike torkance reverses sign near $\Gamma \simeq 20$ meV, whereas in Fe_3GaTe_2 it remains positive throughout.

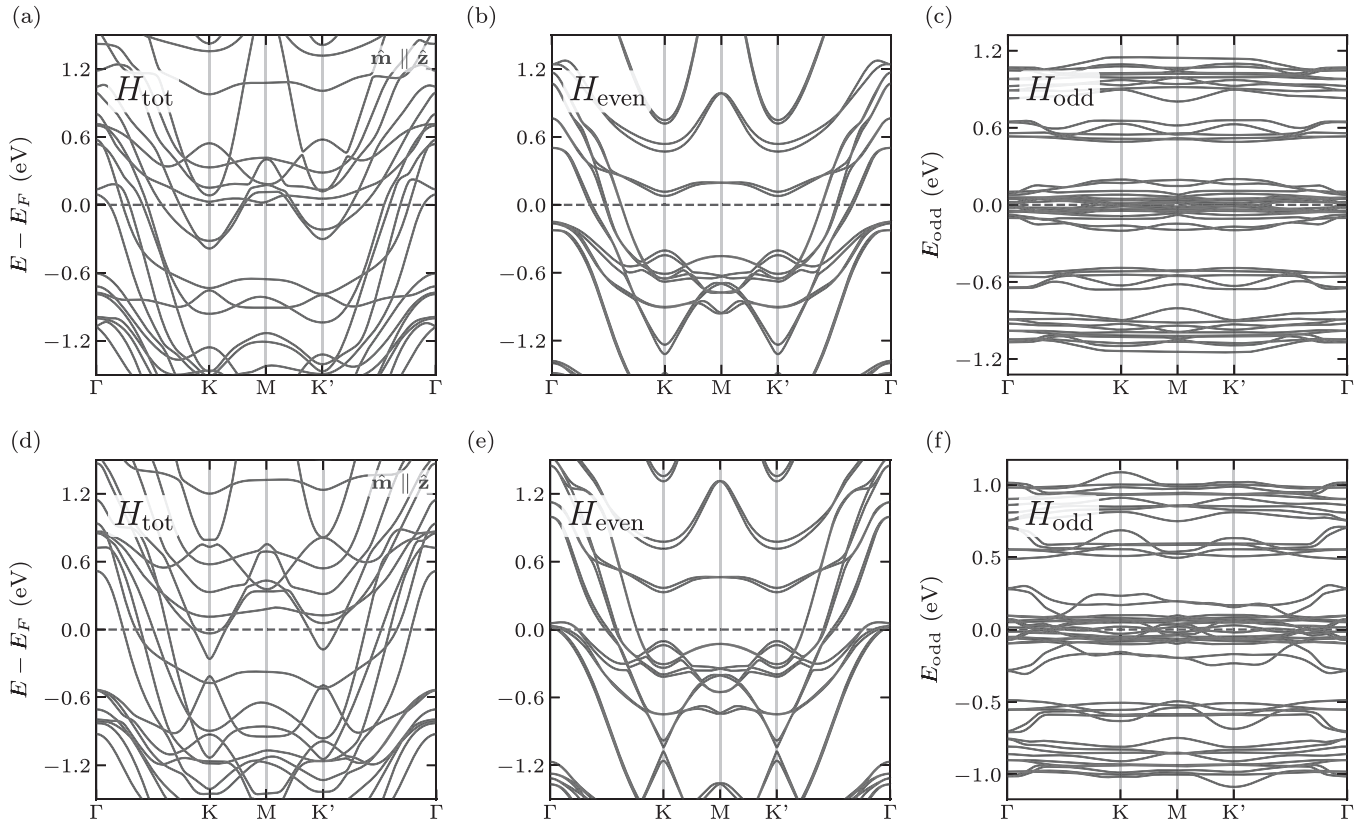


FIG. 7. Band decomposition of monolayer Fe_3GeTe_2 [(a)–(c)] and Fe_3GaTe_2 [(d)–(f)] at $\hat{\mathbf{m}} = \hat{z}$: spectra of the full Hamiltonian, its TR-even component, and its TR-odd component [Eq. (B3)]. The dashed line marks the Fermi level of the full Hamiltonian, repeated on the $H_{\rm even}$ panel as an energy reference; the $H_{\rm odd}$ spectrum is centered on zero and carries no filling of its own. Its narrow bandwidth [(c),(f)] reflects the exchange scale, small compared with the full *p*–*d* dispersion.

and "TR-odd/Fermi-surface" interchangeably. The unrestricted sum in Eq. (C3) retains the diagonal $n = m$ terms, which dominate $t^{\rm odd}$ in the clean limit and generate its Γ^{-1} scaling.

Broadening dependence

The constant broadening Γ of Eqs. (C2) and (C3) corresponds to an effective elastic relaxation time $\Gamma = \hbar/(2\tau_{\rm rel})$. Following Refs. [32,33] we treat it as a physical input encoding the impurity content. Figure 6 shows $t_{zx}^{\rm even}$ and $t_{xx}^{\rm odd}$ versus Γ at $\hat{\mathbf{m}} = \hat{\mathbf{y}}$, $\mathbf{E} \parallel \hat{\mathbf{x}}$, evaluated as outlined in Appendix B 3, on the same 800×800 mesh and at the same chemical potentials as the main-text sweeps.

The Fermi-surface component decreases monotonically in both materials, approximately as $1/\Gamma$, drifting upward at larger Γ as interband corrections to the dominant intraband term of Eq. (C3) grow. The wider window in Fe_3GaTe_2 follows from its larger interband splittings near ε_F (Appendix F). The Fermi-sea component is nonmonotonic in both, with a maximum in the range $\Gamma \sim 25$–50 meV, but differs in sign structure: $t_{zx}^{\rm even}$ is negative at small Γ in Fe_3GeTe_2, changes sign near $\Gamma \approx 20$ meV and peaks at $8.7 \times 10^{-3}\, ea_0$, whereas in Fe_3GaTe_2 it remains positive throughout. This reflects the competing signs of the surface-surface, surface-sea and sea-sea terms of Eq. (C2), whose cancellation shifts continuously with Γ. For all angular sweeps we adopt $\Gamma = 10$ meV ($\tau_{\rm rel} \approx 33$ fs).

APPENDIX D: NONCOLLINEAR CONTENT OF $H_{\rm odd}$ AND ITS RESPONSE-LEVEL CONSEQUENCES

Figure 7 shows the spectra of the full Hamiltonian and of its TR-even and TR-odd components [Eq. (B3)] at $\hat{\mathbf{m}} \parallel \hat{\mathbf{z}}$; the $H_{\rm odd}$ spectrum is centered on zero and confined to the exchange scale. Without SOC, $H_{\rm odd}$ at the reference $\hat{\mathbf{m}} = \hat{z}$ would be block diagonal in the two spin sectors (Appendix B 3). Because the Wannier Hamiltonian is built from relativistic spinors, the extracted $H_{\rm odd}$ [Eq. (B3)] carries additional spin-flip entries, the noncollinear content which is removed by the projection of Eq. (B7). We quantify this content by the effective deviation of the projected and unprojected odd Hamiltonians, measured using the Frobenius norm, $\|A\|_F = \sqrt{\mathrm{Tr}(A^\dagger A)}$,

$$R_{\rm nc} = \frac{\left[\sum_{\mathbf{k}} \left\| H_{\rm odd}(\mathbf{k}) - H_{\rm odd}^{\rm proj}(\mathbf{k}) \right\|_F^2\right]^{1/2}}{\left[\sum_{\mathbf{k}} \left\| H_{\rm odd}(\mathbf{k}) \right\|_F^2\right]^{1/2}}. \tag{D1}$$

The scaling of $R_{\rm nc}$ with the Wannier mesh is given in Table II. Refining from $6 \times 6 \times 1$ to $12 \times 12 \times 1$ reduces $R_{\rm nc}$ from 1.31% to 0.95%, staying below 1% for finer mesh sizes. We can thus characterize $H_{\rm odd}$ along $\hat{z}$ as a predominantly collinear-exchange Hamiltonian carrying $\lesssim 1\%$ SOC-induced noncollinear terms.

As already stated, we project $H_{\rm odd}$ to the pure spin sectors, removing the spin-flip content, but only in the torque operator.

TABLE II. Convergence of the noncollinear content R_{nc} [Eq. (D1)] for monolayer Fe_3GeTe_2 with respect to the *ab initio*/Wannierization **k** mesh, converging to ≈0.9%. R_{nc} depends only on the mesh used to build the Wannier model.

DFT/Wannier mesh	R_{nc} (%)
6 × 6 × 1	1.31
12 × 12 × 1	0.95
24 × 24 × 1	0.92
48 × 48 × 1	0.90

The electronic band states derive from the full rotated Hamiltonian (Appendix B 4), with the spin-flip terms present. Since the spin-flip terms are not subject to the rigid magnetization rotation, the Bloch states, and with them the response, acquire a weak rotation-path dependence. All torkance data reported here are therefore little-group symmetrized, removing the symmetry-forbidden components exactly while leaving the allowed channels unchanged.

APPENDIX E: BENCHMARK OF THE RIGID-EXCHANGE ROTATION METHOD

1. Symmetry validation and the Berry-connection contribution

With $\hat{\mathbf{m}}$ in the yz plane the magnetic point group contains $\sigma_{yz}\cdot\hat{\Theta}$, with σ_{yz} the mirror with the normal $\hat{\mathbf{x}}$ and time-reversal $\hat{\Theta}$ from Appendix B 2: σ_{yz} alone reverses any $\hat{\mathbf{m}}$ in that plane, so only the product leaves it invariant. It reverses E_x and, through the TR parity of each Kubo channel, acts with opposite overall sign on the torque pseudovector in the Fermi-sea and Fermi-surface channels, so that preservation of $\tau_a = \sum_b t_{ab}E_b$ [Eq. (1)] forces, for $\mathbf{E} \parallel \hat{\mathbf{x}}$,

$$t_{xx}^{\text{even}} = t_{yx}^{\text{odd}} = t_{zx}^{\text{odd}} = 0. \tag{E1}$$

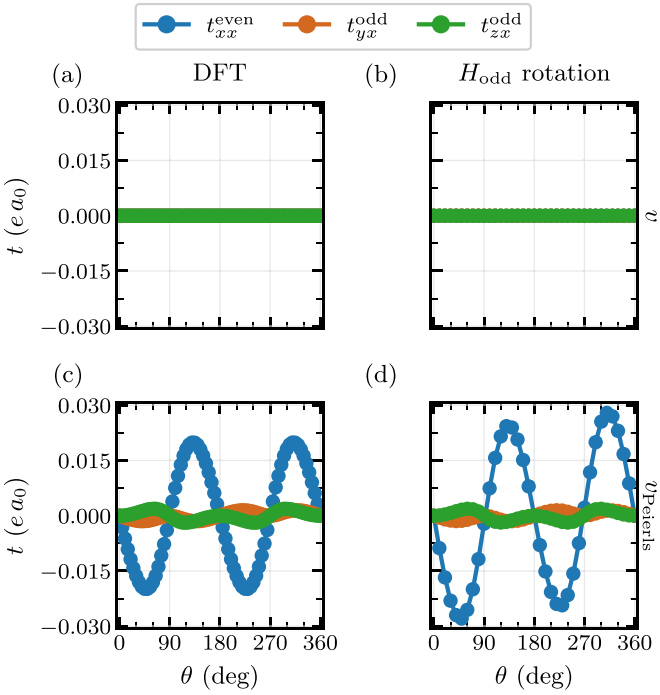


FIG. 8. Symmetry-protected torkance components of monolayer Fe_3GeTe_2 versus the polar angle θ of $\hat{\mathbf{m}}$ in the yz plane, at $\Gamma = 10\,\text{meV}$, $\varepsilon_F = -4.2019\,\text{eV}$, an 800 × 800 × 1 **k** mesh, and $\mathbf{E} \parallel \hat{\mathbf{x}}$. The components t_{xx}^{even} (blue, solid), t_{yx}^{odd} (orange, dashed) and t_{zx}^{odd} (green, dotted) are forbidden by $\sigma_{yz}\hat{\Theta}$ [Eq. (E1)]. They vanish with the full velocity (a),(b), whereas dropping the Berry term (c),(d) generates a spurious t_{xx}^{even} of order $2\times10^{-2}\,e\,a_0$, confirming that the symmetry is carried by the velocity operator and not by the Hamiltonian alone.

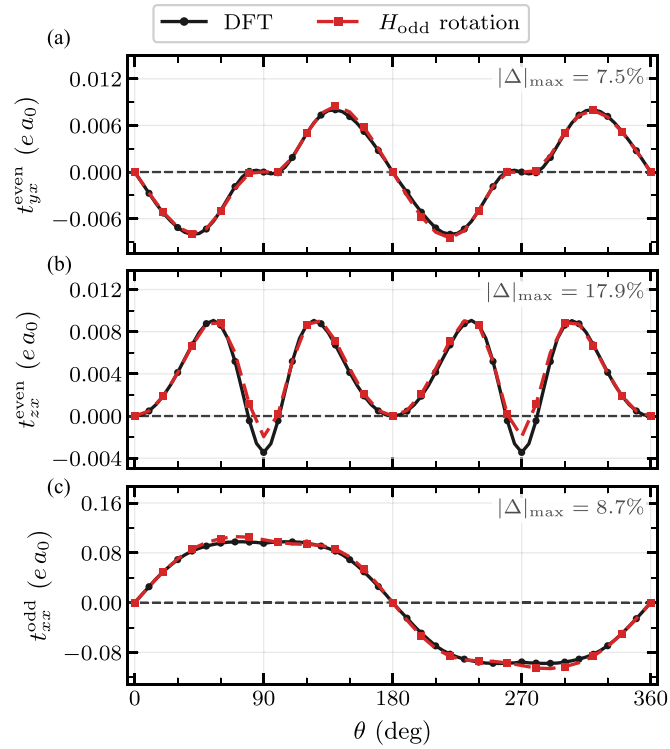


FIG. 9. Rigid-exchange rotation versus self-consistent noncollinear DFT for the three allowed torkance components at $\mathbf{E} \parallel \hat{\mathbf{x}}$ and $\hat{\mathbf{m}}$ in the yz plane [Eq. (E2)]. (a)–(c), top to bottom: t_{yx}^{even}, t_{zx}^{even}, and t_{xx}^{odd} from DFT at each angle (black circles, solid) and from rigid SU(2) rotation of a single reference calculation (red squares, dashed). Each panel quotes the peak relative deviation $|\Delta|_{\max}$ over the sweep, normalized to the largest $|t^{\text{DFT}}|$ of that component [Eq. (E3)]. Full velocity, $\Gamma = 10\,\text{meV}$, $\varepsilon_F = -4.2019\,\text{eV}$, 800 × 800 mesh.

Figure 8 monitors them against the polar angle θ for $H_{\text{odd}}(\hat{\mathbf{m}})$ from self-consistent DFT and from rigid rotation, each evaluated with the full Wannier-gauge velocity of Eq. (A3) and with the Peierls-only velocity $\partial_\alpha H^W/\hbar$. With the full velocity, all three torkances remain below $5\times10^{-5}\,ea_0$ in both schemes—two orders of magnitude below the peak allowed Fermi-sea torkance (≈$9\times10^{-3}\,ea_0$) and three below the fieldlike component (≈$0.1\,ea_0$). However, using only the Peierls velocity, without the gauge terms, would violate the symmetry, leading to $|t_{xx}^{\text{even}}|$ reaching ∼$2\times10^{-2}\,ea_0$—larger than the allowed Fermi-sea response itself—and $|t_{yx}^{\text{odd}}|$, $|t_{zx}^{\text{odd}}|$ reaching ∼$2\times10^{-3}\,ea_0$.

This demonstration makes explicit the use of gauge covariant expressions [58,61,62]: The Berry commutator $i[H^W, \mathcal{A}_\alpha^W]$ [Eq. (A2)] generates the interband velocity matrix elements [Eq. (A6)] that carry the point-group constraints into the response, whereas the Peierls term does not include

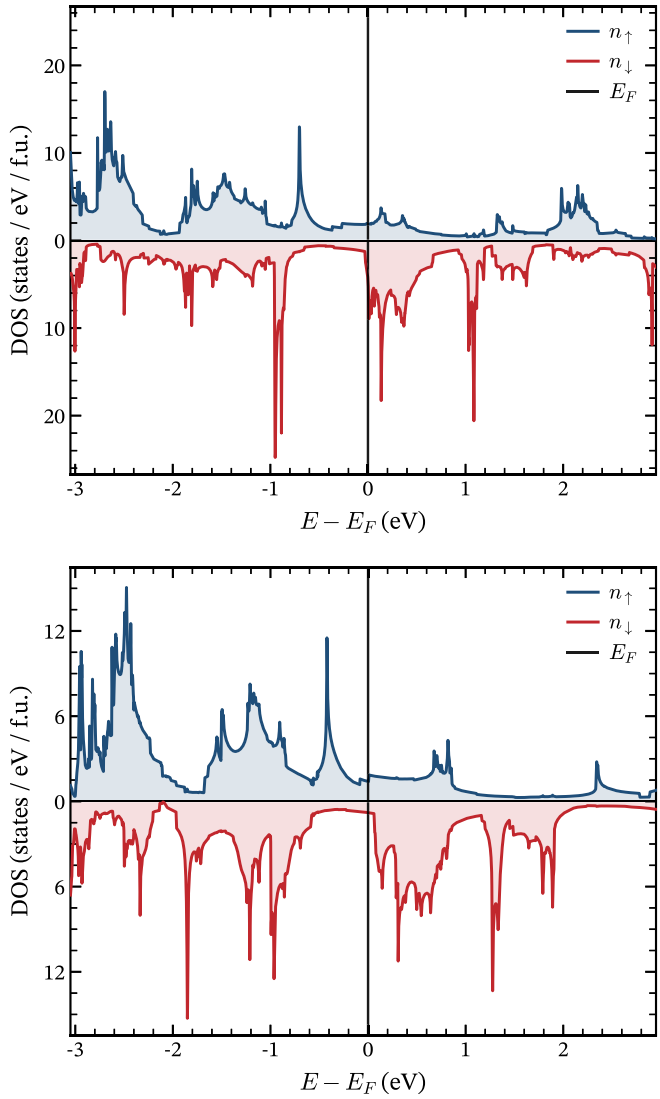


FIG. 10. Calculated spin-resolved DOS of monolayer Fe_3GeTe_2 (top) and Fe_3GaTe_2 (bottom) at $\hat{\mathbf{m}} \parallel \hat{\mathbf{z}}$, with majority ($\langle S_z \rangle > 0$) and minority (plotted downward) channels and $E = 0$ at each compound's Fermi level. In Fe_3GeTe_2 the Fermi level sits at the onset of a sharp, purely minority feature; in Fe_3GaTe_2 the spectrum around ε_F is smooth and majority dominated.

the Wannier centers and transforms covariantly only under **k**-independent basis changes. All torkances in this work therefore use the full velocity of Eq. (A3).

2. Equivalence with self-consistent DFT

The rigid-rotation method holds H_{even} fixed and rotates only the exchange field of H_{odd} [Appendix B 3]; it is valid if the $\hat{\mathbf{m}}$ dependence of H_{even}, entering solely through spin-orbit coupling, is much weaker than the exchange splitting. We test this method against full noncollinear DFT, recomputed at each $\hat{\mathbf{m}}$, sweeping

$$\hat{\mathbf{m}}(\theta) = (0,\ \sin\theta,\ \cos\theta) \tag{E2}$$

with $\Gamma = 10$ meV and an 800×800 mesh. The result for FGT is presented in Fig. 9, demonstrating that both methods agree very well for this yz-plane sweep. We also plot the relative deviation

$$\frac{\Delta(\theta)}{|t^{\text{DFT}}|_{\max}} \equiv \frac{t^{H_{\text{odd}}\text{-rot}}(\theta) - t^{\text{DFT}}(\theta)}{\max_{\theta'} |t^{\text{DFT}}(\theta')|}, \tag{E3}$$

normalized by the peak values. The torques in Figs. 9(a) and 9(c) agree to $\lesssim 5\%$ over most of the range, with local peaks of $\sim 7\%$ near $\theta \approx 150^\circ, 210^\circ$ and $\sim 9\%$ near $\theta \approx 70^\circ, 290^\circ$.

The even t_{zx}^{even} [Fig. 9(b)] is the exception: At $\theta \approx 90^\circ, 270^\circ$ the deviation reaches $\sim 17\%$, an absolute $\approx 2.6 \times 10^{-3}\, ea_0$ against a local DFT value of $-3.45 \times 10^{-3}\, ea_0$. This is not unexpected, given that the rigid rotation starts by freezing the spin-flip components of the exchange Hamiltonian at $\theta = 0$.

Most importantly, the agreement of the rigid rotation and full DFT extends to the harmonic content: $t_{zx}^{\text{even}}(\theta)$ shows four extrema with symmetry-forced zeros at the poles, and the rigid rotation reproduces their positions and relative magnitudes. We thus adopt the rigid-rotation method for all dense angular sweeps to obtain full spherical maps of the torques, while recognizing its inherent numerical inaccuracies.

APPENDIX F: SPIN-RESOLVED DENSITY OF STATES

For completeness, we also report the spin-resolved density of states (DOS). The two ferromagnets differ at ε_F in both magnitude and spin character (Fig. 10). In FGT the total DOS is $N(\varepsilon_F) = 6.46\ \text{eV}^{-1}$ ($n_\uparrow = 1.90$, $n_\downarrow = 4.55\ \text{eV}^{-1}$), a minoritylike polarization $P = -0.41$, with ε_F at the edge of a steep, purely minority feature: $n_\downarrow$ grows by a factor 3.8 over the 50 meV below ε_F and peaks in slope 5 meV above it, while $n_\uparrow$ stays flat near $1.9\ \text{eV}^{-1}$. The feature survives the transport broadening ($P = -0.44$ at $\Gamma = 10$ meV).

In contrast, FGaT has a smaller DOS: $N(\varepsilon_F) = 2.21\ \text{eV}^{-1}$ ($n_\uparrow = 1.41$, $n_\downarrow = 0.80$) and majoritylike spin polarization, $P = +0.28$. The substitution of Ge by Ga thus reduces the Fermi-level DOS nearly threefold and interchanges its spin character. This should be manifested in spin-polarized tunneling experiments.

[1] I. Žutić, J. Fabian, and S. Das Sarma, Spintronics: Fundamentals and applications, Rev. Mod. Phys. **76**, 323 (2004).
[2] J. Slonczewski, Current-driven excitation of magnetic multilayers, J. Magn. Magn. Mater. **159**, L1 (1996).
[3] L. Berger, Emission of spin waves by a magnetic multilayer traversed by a current, Phys. Rev. B **54**, 9353 (1996).
[4] J. A. Katine, F. J. Albert, R. A. Buhrman, E. B. Myers, and D. C. Ralph, Current-driven magnetization reversal and

spin-wave excitations in Co/Cu/Co pillars, Phys. Rev. Lett. **84**, 3149 (2000).

[5] V. Edelstein, Spin polarization of conduction electrons induced by electric current in two-dimensional asymmetric electron systems, Solid State Commun. **73**, 233 (1990).

[6] J. Sinova, S. O. Valenzuela, J. Wunderlich, C. H. Back, and T. Jungwirth, Spin Hall effects, Rev. Mod. Phys. **87**, 1213 (2015).

[7] I. Mihai Miron, G. Gaudin, S. Auffret, B. Rodmacq, A. Schuhl, S. Pizzini, J. Vogel, and P. Gambardella, Current-driven spin torque induced by the Rashba effect in a ferromagnetic metal layer, Nat. Mater. **9**, 230 (2010).

[8] I. M. Miron, K. Garello, G. Gaudin, P.-J. Zermatten, M. V. Costache, S. Auffret, S. Bandiera, B. Rodmacq, A. Schuhl, and P. Gambardella, Perpendicular switching of a single ferromagnetic layer induced by in-plane current injection, Nature (London) **476**, 189 (2011).

[9] A. Manchon, J. Železný, I. M. Miron, T. Jungwirth, J. Sinova, A. Thiaville, K. Garello, and P. Gambardella, Current-induced spin-orbit torques in ferromagnetic and antiferromagnetic systems, Rev. Mod. Phys. **91**, 035004 (2019).

[10] B. Huang, G. Clark, E. Navarro-Moratalla, D. R. Klein, R. Cheng, K. L. Seyler, D. Zhong, E. Schmidgall, M. A. McGuire, D. H. Cobden, W. Yao, D. Xiao, P. Jarillo-Herrero, and X. Xu, Layer-dependent ferromagnetism in a van der Waals crystal down to the monolayer limit, Nature (London) **546**, 270 (2017).

[11] C. Gong, L. Li, Z. Li, H. Ji, A. Stern, Y. Xia, T. Cao, W. Bao, C. Wang, Y. Wang, Z. Q. Qiu, R. J. Cava, S. G. Louie, J. Xia, and X. Zhang, Discovery of intrinsic ferromagnetism in two-dimensional van der Waals crystals, Nature (London) **546**, 265 (2017).

[12] Z. Fei, B. Huang, P. Malinowski, W. Wang, T. Song, J. Sanchez, W. Yao, D. Xiao, X. Zhu, A. F. May, W. Wu, D. H. Cobden, J.-H. Chu, and X. Xu, Two-dimensional itinerant ferromagnetism in atomically thin Fe_3GeTe_2, Nat. Mater. **17**, 778 (2018).

[13] Y. Deng, Y. Yu, Y. Song, J. Zhang, N. Z. Wang, Z. Sun, Y. Yi, Y. Z. Wu, S. Wu, J. Zhu, J. Wang, X. H. Chen, and Y. Zhang, Gate-tunable room-temperature ferromagnetism in two-dimensional Fe_3GeTe_2, Nature (London) **563**, 94 (2018).

[14] D. MacNeill, G. M. Stiehl, M. H. D. Guimaraes, R. A. Buhrman, J. Park, and D. C. Ralph, Control of spin–orbit torques through crystal symmetry in WTe_2/ferromagnet bilayers, Nat. Phys. **13**, 300 (2017).

[15] I.-H. Kao, R. Muzzio, H. Zhang, M. Zhu, J. Gobbo, S. Yuan, D. Weber, R. Rao, J. Li, J. H. Edgar, J. E. Goldberger, J. Yan, D. G. Mandrus, J. Hwang, R. Cheng, J. Katoch, and S. Singh, Deterministic switching of a perpendicularly polarized magnet using unconventional spin–orbit torques in WTe_2, Nat. Mater. **21**, 1029 (2022).

[16] R. Roemer, C. Liu, and K. Zou, Robust ferromagnetism in wafer-scale monolayer and multilayer Fe_3GeTe_2, npj 2D Mater Appl **4**, 33 (2020).

[17] G. Zhang, F. Guo, H. Wu, X. Wen, L. Yang, W. Jin, W. Zhang, and H. Chang, Above-room-temperature strong intrinsic ferromagnetism in 2D van der Waals Fe_3GaTe_2 with large perpendicular magnetic anisotropy, Nat. Commun. **13**, 5067 (2022).

[18] A. M. Ruiz, D. L. Esteras, D. López-Alcalá, and J. J. Baldoví, On the origin of the above-room-temperature magnetism in the 2D van der Waals ferromagnet Fe_3GaTe_2, Nano Lett. **24**, 7886 (2024).

[19] M. Alghamdi, M. Lohmann, J. Li, P. R. Jothi, Q. Shao, M. Aldosary, T. Su, B. P. T. Fokwa, and J. Shi, Highly efficient spin–orbit torque and switching of layered ferromagnet Fe_3GeTe_2, Nano Lett. **19**, 4400 (2019).

[20] X. Wang, J. Tang, X. Xia, C. He, J. Zhang, Y. Liu, C. Wan, C. Fang, C. Guo, W. Yang, Y. Guang, X. Zhang, H. Xu, J. Wei, M. Liao, X. Lu, J. Feng, X. Li, Y. Peng, H. Wei, *et al.*, Current-driven magnetization switching in a van der Waals ferromagnet Fe_3GeTe_2, Sci. Adv. **5**, eaaw8904 (2019).

[21] H. Wang, H. Wu, J. Zhang, Y. Liu, D. Chen, C. Pandey, J. Yin, D. Wei, N. Lei, S. Shi, H. Lu, P. Li, A. Fert, K. L. Wang, T. Nie, and W. Zhao, Room temperature energy-efficient spin-orbit torque switching in two-dimensional van der Waals Fe_3GeTe_2 induced by topological insulators, Nat. Commun. **14**, 5173 (2023).

[22] S. N. Kajale, T. Nguyen, C. A. Chao, D. C. Bono, A. Boonkird, M. Li, and D. Sarkar, Current-induced switching of a van der Waals ferromagnet at room temperature, Nat. Commun. **15**, 1485 (2024).

[23] P. R. Sharma, B. Jang, G. Zhang, W. Jin, H. Chang, and J. Hong, Field-free highly efficient spin-orbit torque switching in Fe_3GaTe_2 at room temperature enabled by a unique distorted crystal symmetry of WTe_2, Appl. Surf. Sci. Adv. **29**, 100847 (2025).

[24] D. Zhang, H. Wei, J. Duan, J. Chen, J. Chen, D. Yue, W. Gong, P. Liu, Y. Yang, J. Gou, J. Yan, K. Zhai, P. Wang, S. Hu, Z. Jia, W. Jiang, L. Liu, W. Wang, Y. Li, and Y. Jiang, Orbital torque switching of room temperature two-dimensional van der Waals ferromagnet Fe_3GaTe_2, Nat. Commun. **16**, 7047 (2025).

[25] L. Pandey, B. Zhao, K. Tenzin, R. Ngaloy, V. Lamparská, H. Bangar, A. Ali, M. Abdel-Hafiez, G. Zhang, H. Wu, H. Chang, L. Sjöström, P. Rout, J. Sławińska, and S. P. Dash, Tunable unconventional spin orbit torque magnetization dynamics in van der Waals heterostructures, Nat. Commun. **16**, 8722 (2025).

[26] Ø. Johansen, V. Risinggård, A. Sudbø, J. Linder, and A. Brataas, Current control of magnetism in two-dimensional Fe_3GeTe_2, Phys. Rev. Lett. **122**, 217203 (2019).

[27] F. Martin, K. Lee, M. Schmitt, A. Liedtke, A. Shahee, H. T. Simensen, T. Scholz, T. G. Saunderson, D. Go, M. Gradhand, Y. Mokrousov, T. Denneulin, A. Kovács, B. Lotsch, A. Brataas, and M. Kläui, Strong bulk spin–orbit torques quantified in the van der Waals ferromagnet Fe_3GeTe_2, Mater. Res. Lett. **11**, 84 (2023).

[28] T. G. Saunderson, D. Go, S. Blügel, M. Kläui, and Y. Mokrousov, Hidden interplay of current-induced spin and orbital torques in bulk Fe_3GeTe_2, Phys. Rev. Res. **4**, L042022 (2022).

[29] J. Železný, H. Gao, K. Výborný, J. Zemen, J. Mašek, A. Manchon, J. Wunderlich, J. Sinova, and T. Jungwirth, Relativistic Néel-order fields induced by electrical current in antiferromagnets, Phys. Rev. Lett. **113**, 157201 (2014).

[30] W. Fang and K. D. Belashchenko, First-principles calculations of spin-orbit torques in Mn_2Au/heavy-metal bilayers, Phys. Rev. B **105**, 064412 (2022).

[31] F. Xue and P. M. Haney, Intrinsic staggered spin-orbit torque for the electrical control of antiferromagnets: Application to CrI_3, Phys. Rev. B **104**, 224414 (2021).

[32] F. Xue, M. D. Stiles, and P. M. Haney, Angular dependence of spin-orbit torque in monolayer Fe_3GeTe_2, Phys. Rev. B **108**, 144422 (2023).

[33] F. Freimuth, S. Blügel, and Y. Mokrousov, Spin-orbit torques in Co/Pt(111) and Mn/W(001) magnetic bilayers from first principles, Phys. Rev. B **90**, 174423 (2014).

[34] P. Giannozzi, S. Baroni, N. Bonini, M. Calandra, R. Car, C. Cavazzoni, D. Ceresoli, G. L. Chiarotti, M. Cococcioni, I. Dabo, A. Dal Corso, S. de Gironcoli, S. Fabris, G. Fratesi, R. Gebauer, U. Gerstmann, C. Gougoussis, A. Kokalj, M. Lazzeri, L. Martin-Samos, *et al.*, QUANTUM ESPRESSO: A modular and open-source software project for quantum simulations of materials, J. Phys.: Condens. Matter **21**, 395502 (2009).

[35] P. Giannozzi, O. Andreussi, T. Brumme, O. Bunau, M. Buongiorno Nardelli, M. Calandra, R. Car, C. Cavazzoni, D. Ceresoli, M. Cococcioni, N. Colonna, I. Carnimeo, A. Dal Corso, S. de Gironcoli, P. Delugas, R. A. DiStasio Jr, A. Ferretti, A. Floris, G. Fratesi, G. Fugallo, *et al.*, Advanced capabilities for materials modelling with QUANTUM ESPRESSO, J. Phys.: Condens. Matter **29**, 465901 (2017).

[36] P. Giannozzi, O. Baseggio, P. Bonfà, D. Brunato, R. Car, I. Carnimeo, C. Cavazzoni, S. de Gironcoli, P. Delugas, F. Ferrari Ruffino, A. Ferretti, N. Marzari, I. Timrov, A. Urru, and S. Baroni, Quantum ESPRESSO toward the exascale, J. Chem. Phys. **152**, 154105 (2020).

[37] D. R. Hamann, Optimized norm-conserving Vanderbilt pseudopotentials, Phys. Rev. B **88**, 085117 (2013).

[38] M. J. van Setten, M. Giantomassi, E. Bousquet, M. J. Verstraete, D. R. Hamann, X. Gonze, and G.-M. Rignanese, The PseudoDojo: Training and grading a 85 element optimized norm-conserving pseudopotential table, Comput. Phys. Commun. **226**, 39 (2018).

[39] S. Ismail-Beigi, Truncation of periodic image interactions for confined systems, Phys. Rev. B **73**, 233103 (2006).

[40] T. Sohier, M. Calandra, and F. Mauri, Density functional perturbation theory for gated two-dimensional heterostructures: Theoretical developments and application to flexural phonons in graphene, Phys. Rev. B **96**, 075448 (2017).

[41] J. P. Perdew, K. Burke, and M. Ernzerhof, Generalized gradient approximation made simple, Phys. Rev. Lett. **77**, 3865 (1996).

[42] H.-J. Deiseroth, K. Aleksandrov, C. Reiner, L. Kienle, and R. K. Kremer, Fe_3GeTe_2 and Ni_3GeTe_2 – two new layered transition-metal compounds: Crystal structures, hrtem investigations, and magnetic and electrical properties, Eur. J. Inorg. Chem. **2006**, 1561 (2006).

[43] A. F. May, S. Calder, C. Cantoni, H. Cao, and M. A. McGuire, Magnetic structure and phase stability of the van der Waals bonded ferromagnet $Fe_{3-x}GeTe_2$, Phys. Rev. B **93**, 014411 (2016).

[44] S. Wu, Z. He, M. Gu, L. Ren, J. Li, B. Deng, D. Wang, X. Guo, W. Li, M. Chen, Y. Chen, M. Meng, Q. Ye, B. Shen, X. Chen, J. Guo, G. Xing, I. K. Sou, and S. Li, Robust ferromagnetism in wafer-scale Fe_3GaTe_2 above room-temperature, Nat. Commun. **15**, 10765 (2024).

[45] J. P. Perdew and Y. Wang, Accurate and simple analytic representation of the electron-gas correlation energy, Phys. Rev. B **45**, 13244 (1992).

[46] H. L. Zhuang, P. R. C. Kent, and R. G. Hennig, Strong anisotropy and magnetostriction in the two-dimensional Stoner ferromagnet Fe_3GeTe_2, Phys. Rev. B **93**, 134407 (2016).

[47] J.-X. Zhu, M. Janoschek, D. S. Chaves, J. C. Cezar, T. Durakiewicz, F. Ronning, Y. Sassa, M. Mansson, B. L. Scott, N. Wakeham, E. D. Bauer, and J. D. Thompson, Electronic correlation and magnetism in the ferromagnetic metal Fe_3GeTe_2, Phys. Rev. B **93**, 144404 (2016).

[48] M. Methfessel and A. T. Paxton, High-precision sampling for Brillouin-zone integration in metals, Phys. Rev. B **40**, 3616 (1989).

[49] R. Sakuma, Symmetry-adapted Wannier functions in the maximal localization procedure, Phys. Rev. B **87**, 235109 (2013).

[50] S. Tsirkin, High performance Wannier interpolation of Berry curvature and related quantities with WannierBerri code, npj Comput. Mater. **7**, 33 (2021).

[51] N. Marzari and D. Vanderbilt, Maximally localized generalized Wannier functions for composite energy bands, Phys. Rev. B **56**, 12847 (1997).

[52] I. Souza, N. Marzari, and D. Vanderbilt, Maximally localized Wannier functions for entangled energy bands, Phys. Rev. B **65**, 035109 (2001).

[53] M. Iraola, J. L. Mañes, B. Bradlyn, M. K. Horton, T. Neupert, M. G. Vergniory, and S. S. Tsirkin, Irrep: Symmetry eigenvalues and irreducible representations of *ab initio* band structures, Comput. Phys. Commun. **272**, 108226 (2022).

[54] S. Ghosh, S. Ershadrad, V. Borisov, and B. Sanyal, Unraveling effects of electron correlation in two-dimensional Fe_nGeTe_2 ($n = 3, 4, 5$) by dynamical mean field theory, npj Comput. Mater. **9**, 86 (2023).

[55] B. Chen, J. Yang, H. Wang, M. Imai, H. Ohta, C. Michioka, K. Yoshimura, and M. Fang, Magnetic properties of layered itinerant electron ferromagnet Fe_3GeTe_2, J. Phys. Soc. Jpn. **82**, 124711 (2013).

[56] K. D. Belashchenko, A. A. Kovalev, and M. van Schilfgaarde, Interfacial contributions to spin-orbit torque and magnetoresistance in ferromagnet/heavy-metal bilayers, Phys. Rev. B **101**, 020407(R) (2020).

[57] N. Marzari, A. A. Mostofi, J. R. Yates, I. Souza, and D. Vanderbilt, Maximally localized Wannier functions: Theory and applications, Rev. Mod. Phys. **84**, 1419 (2012).

[58] J. R. Yates, X. Wang, D. Vanderbilt, and I. Souza, Spectral and Fermi surface properties from Wannier interpolation, Phys. Rev. B **75**, 195121 (2007).

[59] D. Vanderbilt, *Berry Phases in Electronic Structure Theory: Electric Polarization, Orbital Magnetization and Topological Insulators* (Cambridge University Press, Cambridge, 2018).

[60] T. Cole, S. Coh, and D. Vanderbilt, Python Tight Binding (PythTB), version 2.0.0, Zenodo (2025), doi:10.5281/zenodo.12721315.

[61] X. Wang, J. R. Yates, I. Souza, and D. Vanderbilt, *Ab initio* calculation of the anomalous Hall conductivity by Wannier interpolation, Phys. Rev. B **74**, 195118 (2006).

[62] D. Go, H.-W. Lee, P. M. Oppeneer, S. Blügel, and Y. Mokrousov, First-principles calculation of orbital Hall effect by Wannier interpolation: Role of orbital dependence of the anomalous position, Phys. Rev. B **109**, 174435 (2024).